Newton

Article

High-performance integrated circularly polarized light detection using soft-helix-decorated perovskite diodes

Graphical abstract

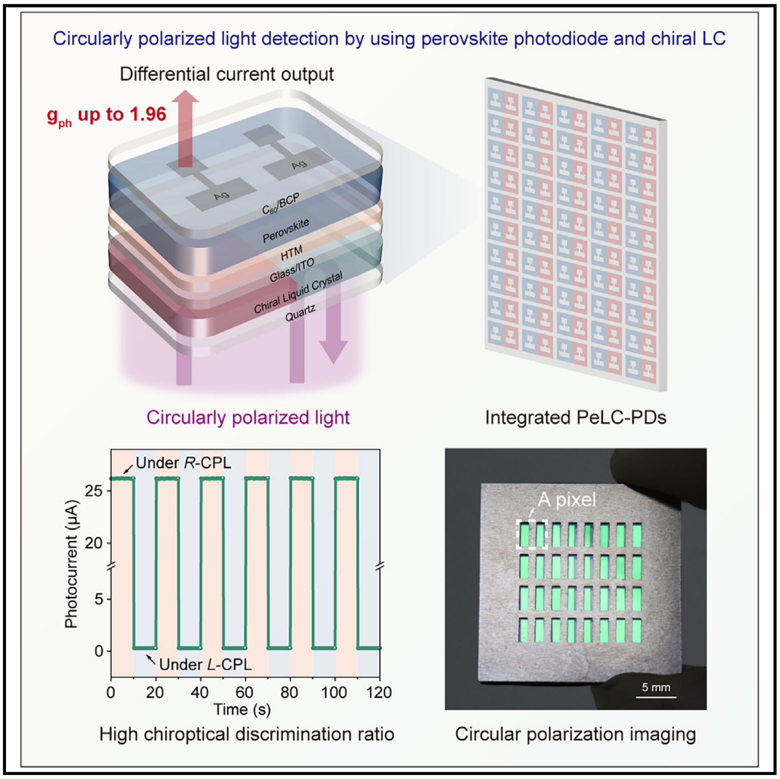

Highlights

- Excellent chiroptical discrimination ability
- Quantitative detection of ellipticity for arbitrary polarized light
- Broadly tunable detection wavelength range and flexible devices
- Easy miniaturization and integration for circular polarization imaging

Authors

Shuaijun Liu, Furong Yu, Xuan Liu, ..., Zhigang Zheng, Yongzhen Wu, Wei-Hong Zhu

Correspondence

zgzheng@ecust.edu.cn (Z.Z.),
wu.yongzhen@ecust.edu.cn (Y.W.),
whzhu@ecust.edu.cn (W.-H.Z.)

In brief

This work presents a circular polarization detector made up of a chiral liquid crystal layer that is sensitive to circular polarization and a perovskite photodiode, resulting in a highly flexible and integrable device that can analyze circularly polarized light with a discrimination ability that exceeds current solutions.

Liu et al., 2025, Newton *1*, 100003
March 3, 2025
https://doi.org/10.1016/j.newton.2024.100003

CellPress

Please cite this article in press as: Liu et al., High-performance integrated circularly polarized light detection using soft-helix-decorated perovskite diodes, Newton (2024), https://doi.org/10.1016/j.newton.2024.100003

Newton

CellPress

Article

High-performance integrated circularly polarized light detection using soft-helix-decorated perovskite diodes

Shuaijun Liu,[1] Furong Yu,[1] Xuan Liu,[2] Huidong Zhang,[1] Minyi Ma,[1] Shuo Zhang,[1] Huanxin Guo,[1] Honglong Hu,[2] Conglong Yuan,[2] Zhigang Zheng,[2,*] Yongzhen Wu,[1,*] and Wei-Hong Zhu[1,3,4,*]

[1]Key Laboratory for Advanced Materials and Joint International Research Laboratory of Precision Chemistry and Molecular Engineering, Shanghai Key Laboratory of Functional Materials Chemistry, Feringa Nobel Prize Scientist Joint Research Center, Institute of Fine Chemicals, Frontiers Science Center for Materiobiology and Dynamic Chemistry, School of Chemistry and Molecular Engineering, East China University of Science and Technology, Shanghai 200237, P.R. China

[2]School of Physics, East China University of Science and Technology, Shanghai 200237, P.R. China

[3]Center of Photosensitive Chemicals Engineering, East China University of Science and Technology, Shanghai 200237, P.R. China

[4]Lead contact

*Correspondence: zgzheng@ecust.edu.cn (Z.Z.), wu.yongzhen@ecust.edu.cn (Y.W.), whzhu@ecust.edu.cn (W.-H.Z.)

https://doi.org/10.1016/j.newton.2024.100003

ACCESSIBLE OVERVIEW Polarization is a property of light describing the plane in which the light wave oscillates as it propagates. In the case of circularly polarized light, this plane rotates as light travels. Circularly polarized light is crucial for many applications, such as quantum communication and computing, as it can be used to encode information. As such, it is important to be able to detect and analyze circularly polarized light. Yet, existing solutions face challenges with miniaturization, integration, and sensitivity, which reduces their applicability. In view of these limitations, this work presents a circular polarization detector made up of a chiral liquid crystal layer that is sensitive to circular polarization and a perovskite photodiode, resulting in a device that can precisely analyze circularly polarized light. Moreover, the device can be adapted to work at different visible wavelengths and integrated into flexible substrates for applications such as wearable devices. The state of polarization can be quantitatively and precisely determined using a pair of these devices, while circular polarization imaging is possible by arranging the devices in an imaging array.

SUMMARY

High-quality circularly polarized light (CPL) detection is essential for many fields, such as optical communication and computing. However, current CPL photodetectors (PDs) face challenges in device integration and exhibit weak circular dichroism, which makes it difficult to precisely determine the polarization state of arbitrarily polarized light. Here, we report a CPL-PD configuration, named PeLC-PD, consisting of a soft helix layer and a perovskite photodiode. PeLC-PD exhibits strong circular dichroism, achieving an anisotropy factor of photocurrent (g_{ph}) up to 1.96 for visible wavelengths, which far exceeds the current state of the art. Quantitative detection of polarization states, including ellipticity and direction of circular polarization, is demonstrated using a paired PeLC-PD layout constructed with a pair of twinned perovskite photodiodes and soft helices of opposite handedness. The paired PeLC-PDs can be used in a pixelated integrated array, thereby enabling circular polarization imaging. Our work resolves a long-standing bottleneck of chiroptical detection and analysis, unlocking the potential for advancements in many fields that depend on precise CPL detection.

INTRODUCTION

Circularly polarized light (CPL), with photons carrying spin angular momentum, plays a pivotal role in various photonic technologies, such as optical quantum communication, polarization-sensitive imaging, and information encryption.[1–3] Detecting CPL is indispensable for a fundamental understanding of chiroptics, including quantum spin, photon resonances, and the precise manipulation of light. Conventional CPL detection (left image in Figure 1A) relies on complicated optical elements like quarter-wave plates (QWPs), linear polarizers, and common optical power meters, which pose challenges in terms of miniaturization

Please cite this article in press as: Liu et al., High-performance integrated circularly polarized light detection using soft-helix-decorated perovskite diodes, Newton (2024), https://doi.org/10.1016/j.newton.2024.100003

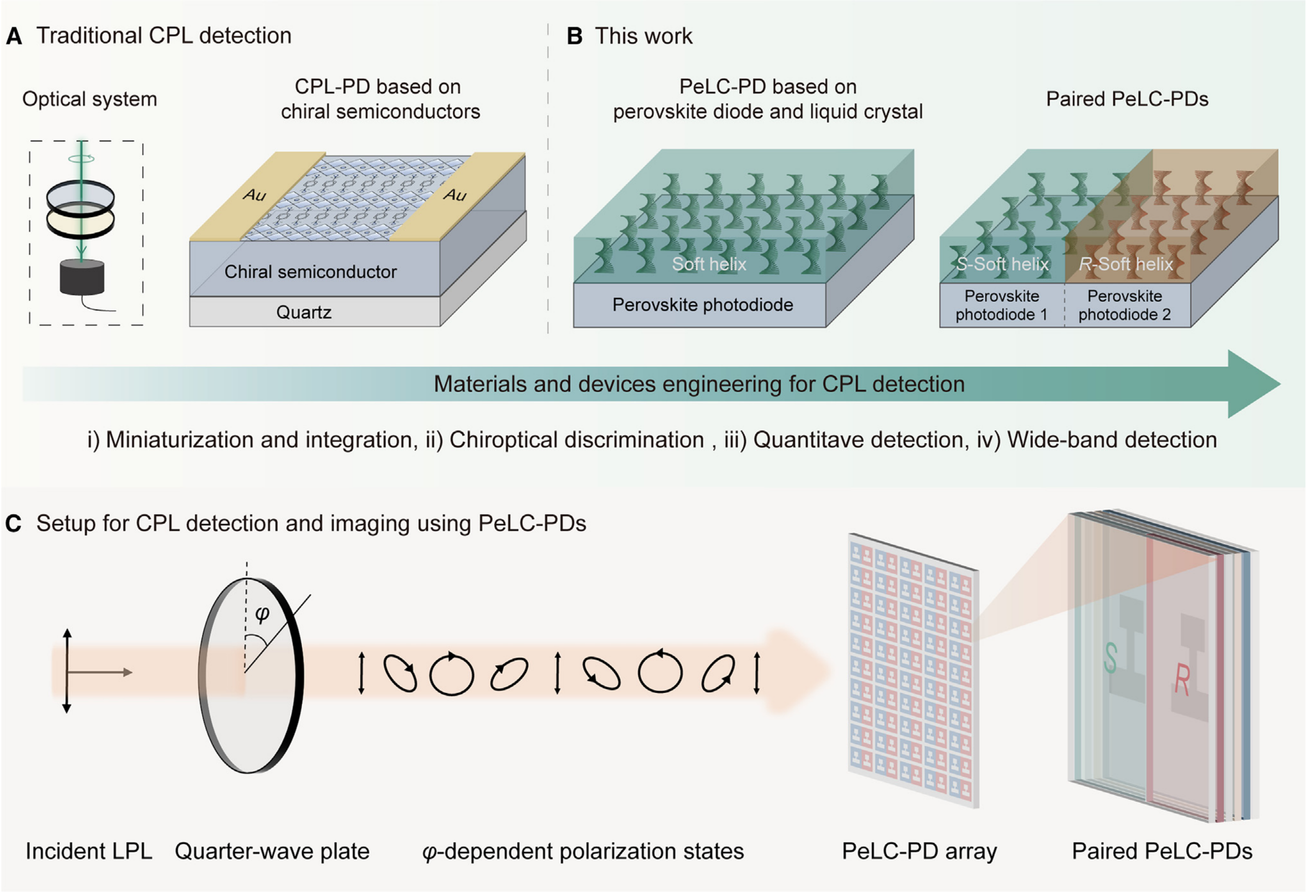

Figure 1. Strategies for CPL detection

(A) Schematic illustration of traditional CPL-PDs based on conventional optical systems and intrinsic chirality-sensitive semiconductors.

(B) Configuration of soft-helix-layer-decorated perovskite photodiode for CPL detection. The device demonstrates remarkable chiroptical discrimination ability, broadly tunable detection wavelength range, easy miniaturization and integration, and quantitative detection of polarization states including linear, elliptical, and circular polarization.

(C) Principle of identification and quantitative detection of CPL by the paired PeLC-PDs in an imaging array. Light with varied polarization states is quantitatively detected by the pixelated PeLC-PD pairs, and the output signals can potentially be utilized to construct high-resolution images with pixelated circular polarization information.

and integration.[4,5] Thin-film CPL photodetectors (CPL-PDs) based on chiral semiconductors, which can directly detect CPL without the need for additional optical elements, is one of the viable strategies to develop CPL detection with simplicity and miniaturization (right image in Figure 1A).[6–16] However, because of the relatively weak circular dichroism (CD) of available chiral semiconductors, these CPL-PDs only generate a tiny electrical difference when exposed to left-handed CPL and right-handed CPL (*L*- and *R*-CPL, respectively) with identical intensity. This is characterized by low values of the anisotropy factor (g_{ph}), which is a key figure-of-merit parameter to evaluate the performance of CPL-PDs that is calculated as $g_{ph} = 2\ (I_L - I_R)/(I_L + I_R)$, where I_L and I_R refer to the photocurrents generated under *L*-CPL and *R*-CPL illumination, respectively.[17,18] Existing CPL-PDs made of chiral semiconductors typically have g_{ph} values below 10^{-1}. Moreover, when the incident light is a single beam and the polarization state is unknown, these CPL-PDs are unable to provide effective polarization information like the direction of the circular polarization and the ellipticity of imperfect CPLs, namely elliptically polarized light.

Chiral liquid crystals (CLCs) are a class of soft helices with one-dimensional (1D) photonic crystals, and they have been demonstrated as fascinating materials for near-perfect modulation of CPL.[19–27] Such a self-assembled helical superstructure selectively transmits CPL with the opposite handedness but reflects CPL with the same handedness in their photonic band gap (PBG)[28–30] and enables precise control of the transmission of CPL. Compared to traditional optical elements like linear polarizers and QWPs, incorporating a CLC layer in perovskite-LC PDs (PeLC-PDs) offers several advantages. First, the self-assembled CLC structure is easier and more cost effective to fabricate. Second, it enables more compact and flexible device designs in complex integrated optical systems. Third, the CLC layer minimizes propagation losses by efficiently manipulating light without increasing the physical path length. While challenges like reproducibility and uniformity arise in large-scale production, they can be addressed in miniaturized devices using advanced deposition techniques such as ink-jet printing. With this in mind, here we present a CPL-PD that combines a CLC-based soft helix layer and a perovskite-based photodiode, named PeLC-PD (left image in Figure 1B). The soft helix acts as a selective filter to *L*-CPL or *R*-CPL, resulting in differential light transmission. The transmitted light signal is further electrically read out by the perovskite photodiode, allowing for the identification between *L*-CPL and *R*-CPL with a g_{ph} value of 1.96, which is a significant improvement over existing solutions. We further propose a unique structure of paired PeLC-PDs for quantitative CPL detection, which comprise a pair of perovskite photodiodes with soft helix layers of opposite handedness (right image in Figure 1B). As verified by the Stokes parameter S_3 extracted from the Poincaré sphere representation, we achieved a precise measurement of ellipticity for arbitrary polarized light by comparing the current output of the paired PeLC-PDs. Such PeLC-PDs can be fabricated on flexible substrates and designed to function for any visible wavelength. We further constructed and demonstrated an imaging array for circular polarization imaging by using the paired PeLC-PDs as pixels (Figure 1C), which paves a promising route to integrable and precise CPL detection for chiral electronics and quantum cryptography in future optical communication and computing systems.

RESULTS

Improving homogeneity and performance of perovskite photodiodes

As mentioned above, the CPL detection by our PeLC-PDs relies on the high chiroptical activity of the soft helix layer and efficient photon-to-electron conversion in the perovskite photodiode. The performance of the photodiode is critical to the final CPL detection capability, especially for integrated devices with paired perovskite photodiodes that carry identical optoelectronic behaviors (Figure 1C). Any deviations in sensitivity between the paired PeLC-PDs will lead to discrepancies in the electrical signal output under the same incident flux, seriously affecting the accuracy of subsequent quantitative circular polarization detection. Therefore, ensuring a consistent and uniform photo-response, i.e., external quantum efficiency (EQE), from the perovskite photodiodes is pivotal to achieving high-precision, quantitative circular polarization detection and further pixelated imaging.

Previous works have emphasized the critical influence of perovskite crystallization quality and film morphology on the performance of perovskite photodiodes,[31,32] in which the hole-transporting layer (HTL) at the bottom of perovskite plays an important role.[33,34] The screening of HTL materials holds promise in improving the detection performance and homogeneity of photodiodes. With this in mind, we selected two commercially available hole-transporting materials (PEDOT:PSS, PTAA) and one homemade molecular hole transporter, (2-(4-(bis(4-methoxyphenyl)amino)phenyl)-1-cyanovinyl)phosphonic acid (MPA-CPA), to fabricate the perovskite photodiodes. The device configuration and molecular structures of hole-transporting materials are shown in Figure 2A, where the MPA-CPA has been proven to efficiently minimize interfacial defects between perovskite and HTL in photovoltaic devices.[35] Three types of devices all exhibit photocurrent responses (obtained at short-circuit conditions) in the wavelength range from 300 to 850 nm (Figure 2B). The EQE plateaus of PEDOT:PSS- and PTAA-based devices are moderate, and their reproducibility is unsatisfactory due to broad-distributed integrated photocurrents. By sharp contrast, the perovskite photodiode based on MPA-CPA exhibits a remarkably improved EQE plateau above 95%, along with better reproducibility of the integrated photocurrents far transcending those based on PEDOT:PSS and PTAA (Figure 2C). These results indicate the superior contribution of MPA-CPA to perovskite thin-film deposition.

To get an insight into the enhanced EQE performance and homogeneity, we carefully compared photodiode devices based on different HTLs. In general, EQE is considered to be affected by the quality and thickness of the perovskite film, which directly impacts the generation and transport of photogenerated carriers.[36–38] Cross-sectional scanning electron microscopy (SEM) images of perovskite photodiodes based on these HTLs show similar thicknesses (~530 nm) of the perovskite layer (Figure S1), ruling out thickness-related effects on EQE variation. The MPA-CPA-based device exhibits better macro-uniformity as revealed by the electroluminescence (EL) images (Figure S2). The crystallinity and morphology of the bottom surface of the perovskite film deposited on different HTLs are further characterized by ultraviolet-visible (UV-vis) absorption, X-ray diffraction (XRD), top-view SEM, and atomic force microscopy (AFM), verifying the enhanced micro-homogeneity and reduced nano-pinhole formation for MPA-CPA-based samples (Figures S3–S7). The MPA-CPA-based perovskite film achieves a Shockley-Read-Hall lifetime of 6.52 μs, which is also much longer than those on PEDOT:PSS and PTAA (Figure S8). The result is consistent with the reduced nano-pinholes observed, further confirming the reduced traps due to the chemical passivation of MPA-CPA to the ionic and deep-level electronic defects. As shown in Figure 2D, the MPA-CPA-based devices also show the lowest dark current density, which is preferable for the sensitivity of photodetection. These results indicate that high-quality contact between the HTL and perovskite can efficiently improve the photoelectric performance of perovskite photodiodes, which is essential to the further design of our CPL-sensitive devices, as shown below.

Decorating perovskite photodiodes with soft helix for CPL detection

The device structure of the proposed CPL-sensitive PeLC-PD is shown in Figure 3A, in which the perovskite photodiode is covered by a 5-μm-thick CLC layer that functions as a soft helix and CPL filter. The detailed fabricating process is described in Figure S9. The CLC can hinder the propagation of the same-handed CPL while permitting the penetration of opposite-handed CPL at wavelengths located in the PBG. Taking a green-light-responsive PeLC-PD as an example, we constructed right- and left-handed CLCs, denoted as *R*-CLCs and *S*-CLCs. Their molecular structures are shown in Figure S10. As illustrated in Figure 3B, the *R*-CLC and *S*-CLC layers show a typical PBG effect from 500 to 560 nm. More importantly, they exhibit opposite CD signals with quite high intensity up to 10^4 mdeg within the PBG (Figure 3C). The anisotropy factor (g_{CD}) is defined

Please cite this article in press as: Liu et al., High-performance integrated circularly polarized light detection using soft-helix-decorated perovskite diodes, Newton (2024), https://doi.org/10.1016/j.newton.2024.100003

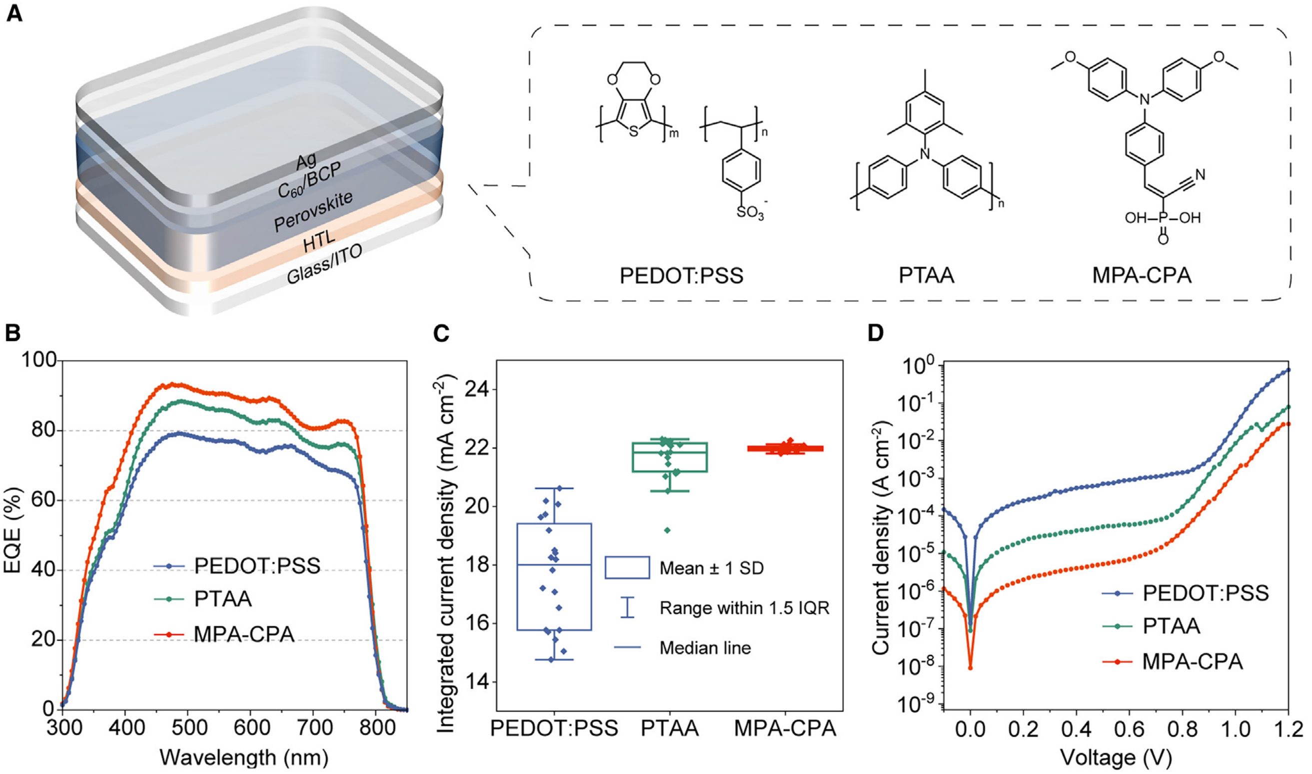

Figure 2. Screening HTLs to improve the detection performance of perovskite photodiodes

(A) Configuration of a perovskite photodiode and the molecular structures of three HTLs, including PEDOT:PSS, PTAA, and MPA-CPA.

(B) EQE spectra of perovskite photodiodes based on three HTLs.

(C) Statistical distribution of integrated current density obtained from EQEs of perovskite photodiodes based on three HTLs (20 devices each).

(D) Dark current density-voltage (*J*-*V*) curves of perovskite photodiodes based on three HTLs.

by $g_{abs} = \Delta\varepsilon/\varepsilon = (A_L - A_R)/A = \mathrm{CD[mdeg]}/(32{,}980\ A)$, where A_L and A_R are the absorbance of left and right CPL, respectively, A is the corresponding absorbance of nonpolarized light, and CD[mdeg] is the chiral intensity of samples. g_{CD} values of CLC layers are calculated to be 1.7 (Figure S11), which is 1–3 orders of magnitude larger than that of the typical chiral semiconductors (10^{-1}–10^{-3} mdeg).[8–10] The result indicates the strong chiroptical discrimination ability of the CLC layer, which is also verified by the simulated transmittance spectra shown in Figures S12 and S13. The *R*-CLC and *S*-CLC show almost 100% transmittance to CPL with opposite handedness while little transmittance to CPL with same handedness, thus enabling the remarkable difference in the photocurrent outputs of the PeLC-PD under *L*-CPL and *R*-CPL illumination. In addition, the perovskite film covered with the CLC layer shows a slightly longer charge carrier lifetime than the pure perovskite film, which stems from the decreased light intensity received by the perovskite film due to the selective reflection of the CLC layer (Figure S14). We also measured the CD spectrum of a pure perovskite film (Figure 3C). As the used perovskite film is achiral, no obvious CD signals are observed, which indicates that excellent discrimination toward CPL stems completely from the CLC layer. The photocurrent of the device without bias potential was measured under pure *L*-CPL and *R*-CPL with varying light intensity from 10^{-1} to 10^{3} μW cm^{-2}, where CPL with opposite handedness is generated from a beam of a green laser (532 nm) followed by a linear polarizer and a QWP. As shown in Figure 3D, the photocurrent of the PeLC-PD with *S*-CLCs under *R*-CPL is two orders of magnitude higher than that under *L*-CPL with identical intensity, hundreds of times larger than the difference in traditional chiral semiconductor-based CPL-PDs. Similarly, the device with *R*-CLCs shows a larger current under *L*-CPL than *R*-CPL (Figure S15). Moreover, the PeLC-PD exhibits a linear photocurrent response to both *L*-CPL and *R*-CPL with varying light intensity from 10^{-1} to 10^{3} μW cm^{-2}, which achieves a linear dynamic range (LDR) of 55 dB (Table S1). The result lays a solid foundation for the subsequent quantitative detection. The device exhibits a g_{ph} value up to 1.96 and a responsivity of 294 mA W^{-1} under light illumination of 1 mW cm^{-2}, which is the highest g_{ph} value among reported CPL-PDs and far transcends CPL-PDs based on chiral semiconductors.[13,39] We further measured the time-dependent photocurrent of the PeLC-PD by switching the incident circular polarization direction (Figure 3E). The large difference in current under *L*-CPL and *R*-CPL confirms the excellent chiral discrimination ability of the device. Also, the constant current under multiple switches of CPL indicates remarkable stability. The demonstration of PeLC-PD breaks the performance limitations of traditional CPL-PDs based on chiral semiconductors, representing a promising route for efficient CPL detection.

Please cite this article in press as: Liu et al., High-performance integrated circularly polarized light detection using soft-helix-decorated perovskite diodes, Newton (2024), https://doi.org/10.1016/j.newton.2024.100003

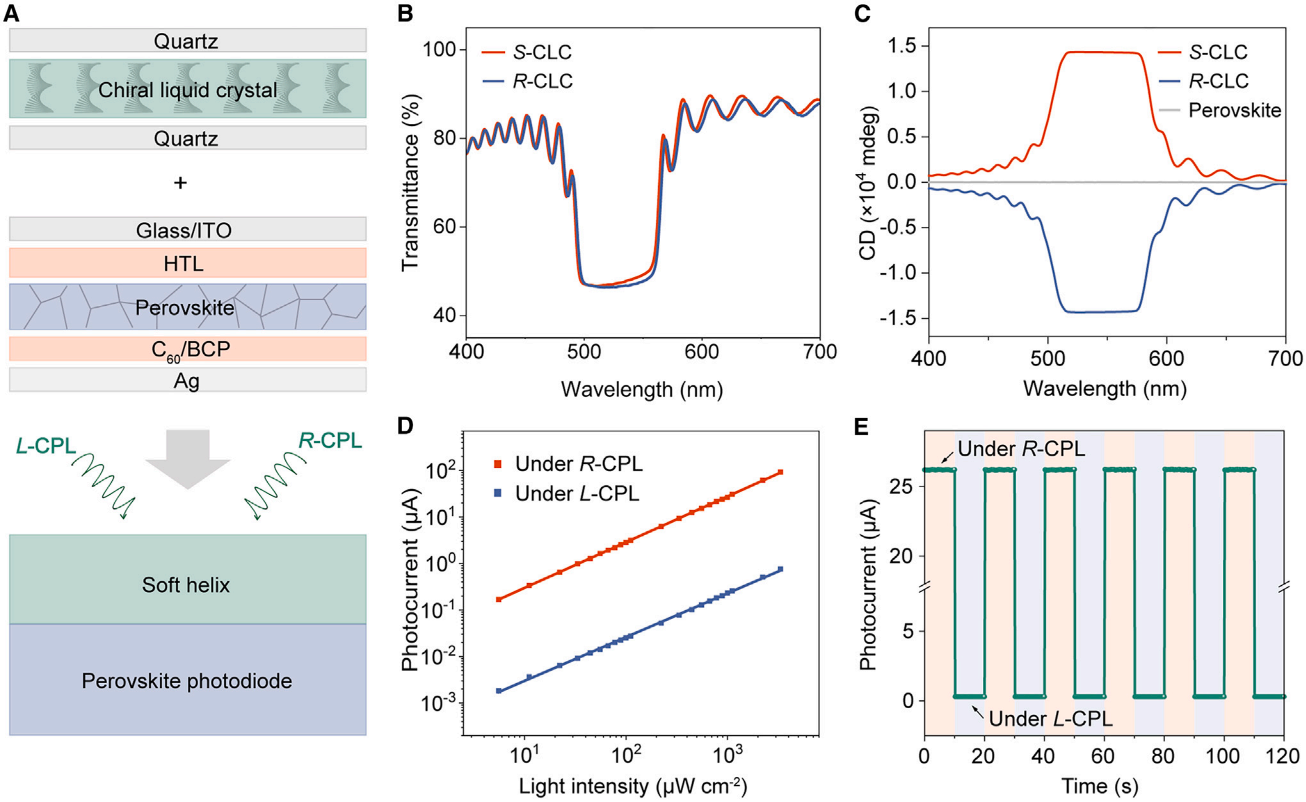

Figure 3. Schematic illustration and performance of PeLC-PD device

(A) Construction of the PeLC-PD by combining a soft helix layer (*R*- or *S*-CLC) and a perovskite photodiode.

(B) Transmittance spectra of the green-light-responsive CLC layer.

(C) CD spectra of the green-light-responsive CLC layer and pure perovskite film.

(D) Photocurrent recorded by the *S*-CLC-based PeLC-PD under *L*- and *R*-CPL with varied intensities (from 10^{-1} to 10^{3} μW cm^{-2}) at 0 V bias.

(E) Time-dependent photocurrent response of the *S*-CLC-based PeLC-PD under alternate *R*-CPL and *L*-CPL irradiation.

Integrating devices for quantifying ellipticity of arbitrary polarized light

Despite the ultrahigh distinguishability to CPL, when facing an unknown polarized light source in practice, it is still challenging for the PeLC-PD to identify circular polarization direction and quantify the ellipticity of incident polarized light. With this in mind, we further designed a green-light-responsive CPL-PD device comprising a pair of twinned perovskite photodiodes and CLC layers of opposite handedness, where the left and right diodes were covered with *S*-CLCs and *R*-CLCs, respectively. The photograph of the real device and its working principle are illustrated in Figures 4A and 4B. Both *R*-CLC and *S*-CLC layers show typical oil-silk textures with remarkably uniform morphology (Figure 4C). The light of arbitrary polarization can be seen as a superposition of left and right CPL, and the CLC reflects one of the CPL components while allowing the other to pass through. Therefore, given the sensitivity in the transmission of the LC layers to CPL of opposite handedness, the twinned perovskite photodiodes will output photocurrents that can be compared to obtain information regarding the direction of circular polarization. For instance, if the device is exposed to a beam of CPL and the current from the left diode is larger than the right diode, then the incident light should be right-handed circular polarization, and vice versa.

In addition to the identification of circular polarization directions, our PeLC-PD device can further quantify the ellipticity of including elliptically and linearly polarized light. Traditionally, this information is acquired from complicated optical systems and processes and expressed by the Stokes parameter S_3 on the Poincaré sphere (see Figure 4F and Note S1 for details).[40–43] S_3 refers to the difference in intensity between *R*- and *L*- CPL; it varies from -1 to 1, in which "$S_3 = 1$" and "$S_3 = -1$" represent pure right- and left-handed circular polarization, respectively, while "$S_3 = 0$" refers to linear polarization. In fact, most of the existing commercial CPL-PDs lack the ability to measure S_3, hindering their practical application in chiroptical detection. As such, we attempt to obtain this information for arbitrary polarized light by using the integrated devices. Thanks to the enhanced uniformity of the perovskite layer, the twinned perovskite photodiodes show almost the same photon-to-electron conversion behavior, i.e., performance synchronism, as revealed by their identical EQE spectra (Figure S16). Moreover, they exhibit a good linear photocurrent response to light intensity across a broad range. These features provide a prerequisite for the integrated device to quantitatively detect the ellipticity of polarized light. As shown in Figure 4E, the right photodiode with *R*-CLCs exhibits

Please cite this article in press as: Liu et al., High-performance integrated circularly polarized light detection using soft-helix-decorated perovskite diodes, Newton (2024), https://doi.org/10.1016/j.newton.2024.100003

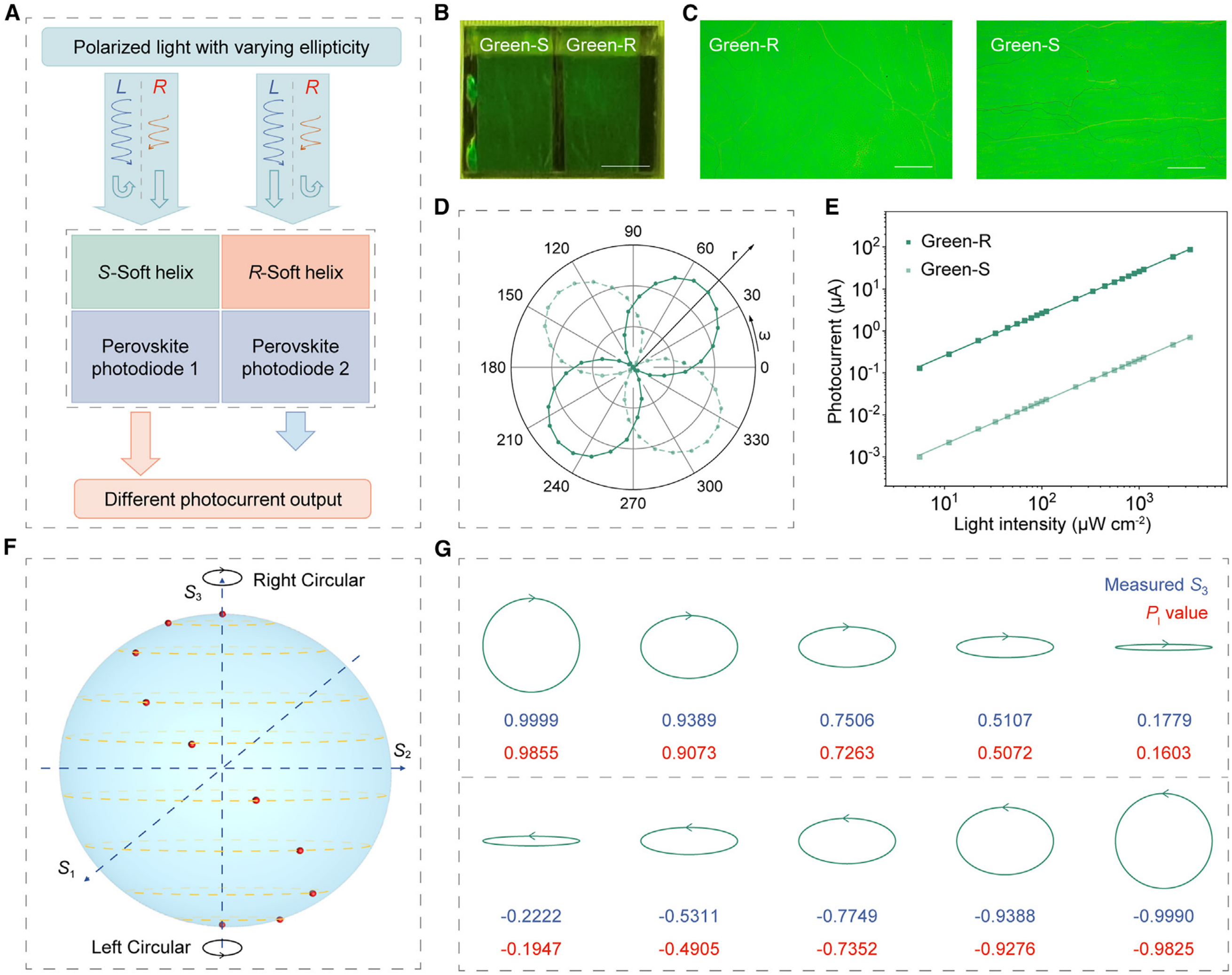

Figure 4. Device engineering for quantitative detection of polarization states

(A) Mechanism and working principle of the paired PeLC-PDs. The different photocurrent outputs of the paired devices under the same polarized light can be used to calculate the ellipticity, which enables quantitative detection of light with varying polarization states.

(B) Photograph of a paired green-light-responsive PeLC-PD. Green-R and green-S subunits use *R*-CLC and *S*-CLC, respectively. Scale bar: 5 mm.

(C) Polarized optical microscopy (POM) images of *R*- and *S*-CLCs integrated in the paired PeLC-PDs measured in reflection mode. Scale bars: 100 μm.

(D) Photocurrent recorded by the paired PeLC-PDs under a green laser beam (1 mW cm^{-2} at 532 nm) with continuously varied polarization states by rotating the angles between the linear polarizer and the QWP from 0° to 360° at an interval of 10° at 0 V bias and plotted in a polar coordinate system. The polar angle ω stands for the transmission angle of the polarizer, and the radius *r* stands for the photocurrent intensity. The solid line and dashed line refer to photocurrents of the PeLC-PDs with *R*-CLCs at the right and *S*-CLCs at the left side, respectively.

(E) Photocurrent response of the paired PeLC-PDs under *L*-CPL and *R*-CPL with varied intensities at 0 V bias.

(F) Poincaré sphere representation for the polarization states.

(G) Comparison of polarization-dependent S_3 (ellipticity) extracted from Poincaré sphere representation and P_l values obtained from the paired PeLC-PDs.

a higher photocurrent than the left one with *S*-CLCs under *L*-CPL illumination. Similarly, the left photodiode with *S*-CLCs exhibits a higher photocurrent than the right one with *R*-CLCs under *R*-CPL (Figure S17). The twinned photodiodes show identical photocurrents under linearly polarized light (Figure S18). In order to describe the polarization state based on photocurrent, we define a circular polarization degree P_l, which can be calculated as $P_l = (I_L - I_R)/(I_L + I_R)$, where I_L and I_R refer to the photocurrents generated from the left and right PeLC-PDs, respectively. Figure 4D shows the polarization-dependent photocurrent of the paired PeLC-PDs, and the twinned perovskite photodiodes exhibit differential photocurrents under varied polarization states, which is further verified by the simulated transmittance (Figure S19). By calculating the P_l values extracted from different photocurrents of the paired PeLC-PDs, we compared them with the Stokes parameter S_3 that was measured by optical elements. As shown in Figure 4G, all the P_l values fit well with the Stokes parameter S_3. These results

Please cite this article in press as: Liu et al., High-performance integrated circularly polarized light detection using soft-helix-decorated perovskite diodes, Newton (2024), https://doi.org/10.1016/j.newton.2024.100003

verify the realization of precise detection of polarized light with integrable and miniaturizable thin-film PDs.

Expanding detection wavelength range

The detection spectral range of traditional CPL-PDs based on chiral semiconductors is severely restricted by a narrow-band chiroptical response. For instance, traditional chiral perovskite- or organic semiconductor-based CPL-PDs only exhibit the cotton effect in a narrow wavelength range (about 100 nm), posing huge difficulties in CPL detection toward practical application. In contrast, the wide-band photo-response of perovskite photodiodes and the facile modulation of the PBG of CLCs endow PeLC-PDs with the capability of broadband CPL detection.[44–46] Here, we further demonstrate blue- and red-light-responsive paired PeLC-PDs by tuning the concentration of chiral dopant in the LC matrix layer. As shown in Figures 5A and 5B, the CLC layers in fabricated PeLC-PDs exhibit varied and uniform reflection color regardless of the chirality, which is consistent with their PBG induced by different helical pitches in the transmittance spectra (Figure S20). Based on the identical working principle of the above-mentioned green-light-responsive PeLC-PD, both *R*- and *S*-CLC-based PeLC-PDs (blue and red) exhibit identical CD intensities and wavelength ranges but opposite signal values (Figure S21), verifying the specific chiroptical discrimination in differential wavelength ranges (Figure S22). As a result, all devices achieve extremely large g_{ph} values above 1.9, demonstrating remarkable CPL-distinguishing capability across the whole visible region (Figure S23; Table S1). Furthermore, these paired devices show opposite variations in polarization-dependent photocurrents against polar angle ω (Figure 5C), which can be used to quantify arbitrary polarization states for blue and red light. The extracted P_{l} values from the blue-, green-, and red-light-responsive paired PeLC-PDs are all well fitted with the Stokes parameter S_3 (Figures 5D–5F). These results manifest the realization of wide-band detection of polarization light, which perfectly overcomes the bottleneck toward wavelength selectivity of traditional CPL-PDs based on chiral semiconductors, further broadening its customizability and applicability.

We further demonstrate the applicability of our strategy in flexible devices. Given the simple solution-based fabrication of perovskite diodes and the soft helix, flexile PeLC-PDs made of perovskite photodiodes and CLC polymers were constructed on an indium tin oxide (ITO)-coated poly(ethylene terephthalate) (PET) substrate (Figures 5G, S24, and S25). Similar to the rigid PeLC-PD, the flexible device exhibits specific EQE responses with varying PBGs of the CLC polymer (Figure S26), confirming the perfect regulation of the CLC polymer to the EQE shape of the perovskite photodiode. The obvious variation in the EQEs of PeLC-PDs based on rigid and flexible substrates stems from the different transmittances of ITO/glass and ITO/PET (Figure S27). These flexible PeLC-PDs also exhibit comparable chiral discrimination abilities and maintain linearity in a broad range (Figures 5H, 5I, and S28), having similar abilities of quantitative detection of arbitrary polarization states (Figures 5J and S29). Such high performance of flexible devices is indicative of their immense potential in diverse application scenarios such as smart wearables, remote sensing, and chiroptical microelectromechanical systems.

Developing integrated arrays for circular polarization imaging

Using the above-mentioned paired PeLC-PDs as pixels, we further construct an integrated array and demonstrate circular polarization imaging (Figure 6A). The array containing 4 × 4 pixels was designed as shown in Figure S30 and fabricated using a modified process. The area of each light-exposing region was kept consistent by covering a metal mask with pre-defined apertures (note that a couple of neighboring apertures correspond to one pixel for CPL imaging; one is *S* and the other is *R*). We demonstrate the circular polarization imaging by building a patterned vector beam that carries a hidden message of "LC" with spatially orthogonal circular polarization states in a 4 × 4 square light spots, and the detailed light path as well as the vector beam are illustrated in Figure 6B. By rotating the QWP behind the vector beam generator, the circular polarization state of each spot can be synchronously switched (Figures 6C and 6D), which can be confirmed by a beam analyzer or a complementary metal-oxide semiconductor (CMOS) camera equipped with a circular polarizer. As the QWP can only change the phase and not the amplitude, the 16 spots with consistent light intensity were simultaneously observed under the CMOS camera (Figure S31). By inserting a left-handed circular polarizer in front of the camera or the beam analyzer, which allows the same-handed CPL to pass through while inhibiting the opposite-handed one, an obvious bright and dark LC pattern appears, demonstrating the construction of the vector beam (Figures 6E–6H).

Encouragingly, such a vector beam can be imaged by our PeLC-PD array without using any additional optical elements. When the PeLC-PD array was exposed to the vector beam, each pixel generated two individual photocurrents, which were used to calculate the P_{l} values. Figures 6I and 6J show the imaging results of the vector beam using the integrated PeLC-PD array. The profile of LC can be clearly captured for both complementary images with opposite contrast colors. This verifies that our PeLC-PD array can clearly distinguish the varied circular polarization state of each light spot in the vector beam, resulting in the successful imaging and restoration of the circular polarization information of the light field. To the best of our knowledge, this is the first time that CPL imaging was realized by thin-film-diode-based PDs. Given the high solution processability of the perovskite and CLCs, our strategy has huge potential for device miniaturization, which not only facilitates easier integration into existing systems but also improves sensitivity and responsivity due to reduced path lengths for light interaction. We believe that the precise miniaturization of micro-devices can be further achieved through advanced techniques such as photolithography and ink-jet printing, paving a promising route to integrable and precise CPL detection for quantum information processing and quantum cryptography in next-generation optical communication and computing systems.

DISCUSSION

Considering the complexity, miniaturization, and integration challenges from conventional CPL detection with complicated optical elements like QWPs, linear polarizers, and common optical power meters, we have developed a high-performance and integrable CPL-PD configuration that combines perovskite photodiodes

Please cite this article in press as: Liu et al., High-performance integrated circularly polarized light detection using soft-helix-decorated perovskite diodes, Newton (2024), https://doi.org/10.1016/j.newton.2024.100003

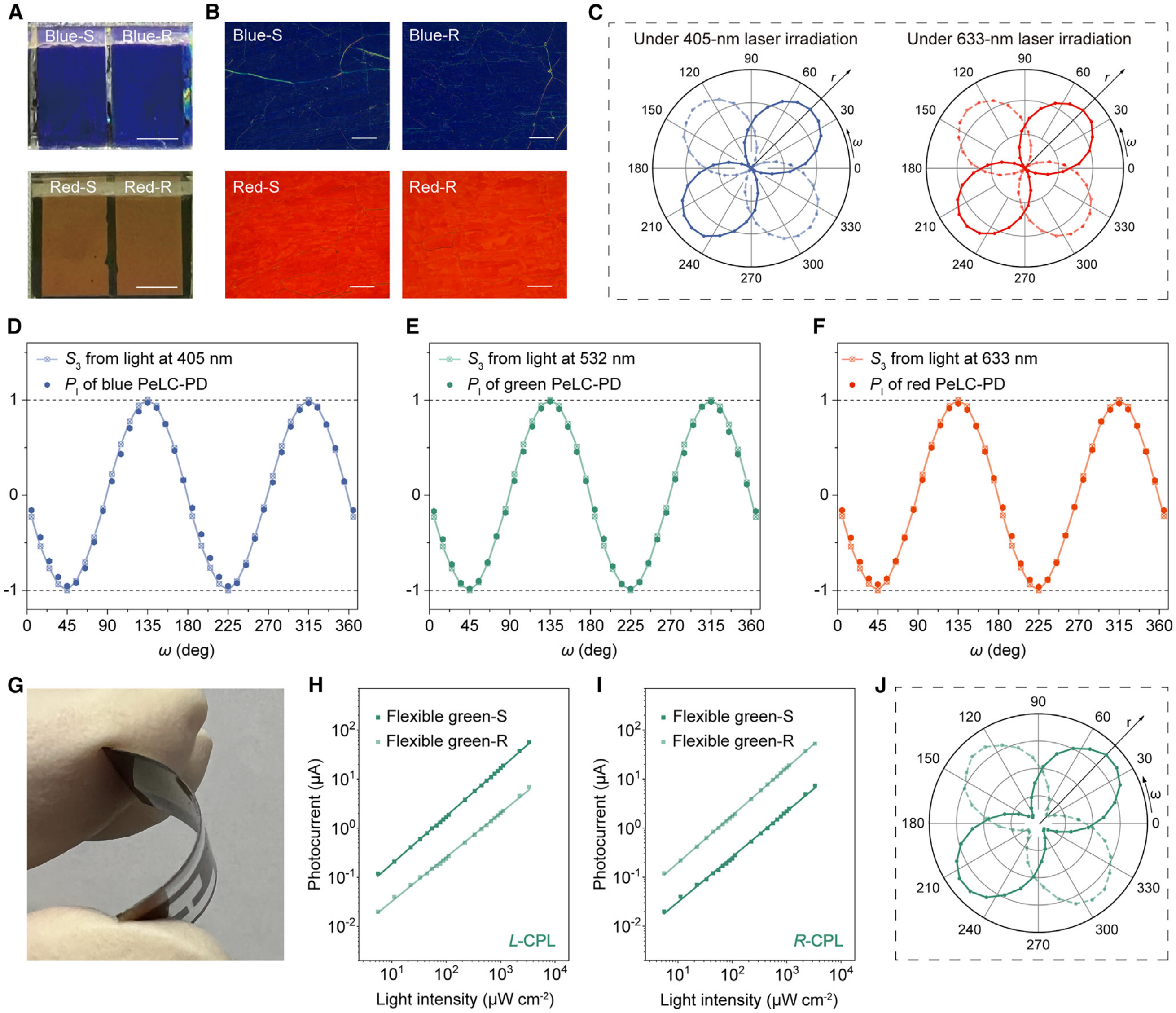

Figure 5. Tunable detection wavelength range and flexible PeLC-PD device

(A) Photographs of blue- and red-light-responsive PeLC-PDs. Scale bars: 5 mm.

(B) POM images of CLC in the PeLC-PDs measured in a reflection mode. Scale bars: 100 μm.

(C) Polarization-dependent photocurrent recorded by the blue- and red-light-responsive PeLC-PDs in a polar coordination system. The solid line and dashed line refer to the photocurrents from PeLC-PD device based on *R*-CLCs at the right and *S*-CLCs at the left side, respectively. The incident light is a laser beam (405 or 633 nm) with a power of 1 mW cm^{-2}.

(D–F) Comparison of P_l values (dark dots) obtained from the PeLC-PDs and S_3 (shallow lines) extracted from Poincaré sphere representation.

(G) Photograph of a flexible green-light-responsive PeLC-PD.

(H and I) Photocurrent response of the flexible PeLC-PDs at 0 V bias under *L*-CPL and *R*-CPL with varied intensities.

(J) Polarization-dependent photocurrent recorded by the flexible PeLC-PDs.

and CLCs (PeLC-PD). Using CLCs, a class of soft helices with 1D photonic crystals, the proposed prototype exhibits remarkable chiroptical discrimination ability with a large anisotropy factor of photocurrent up to 1.96, which significantly surpasses the performance of current chiral semiconductor-based CPL-PDs. By utilizing a pair of twinned perovskite photodiodes and soft helices of opposite handedness, we successfully realized the quantitative detection of ellipticity for arbitrarily polarized light, as verified by the Stokes parameters S_3 extracted from the Poincaré sphere. In addition, we demonstrated the adaptability of the PeLC-PDs by customizing them to function for different visible wavelengths, as well as integrating them onto flexible substrates to achieve flexile devices with detection performance comparable to their rigid counterparts. We further showed that the paired PeLC-PDs can be used as pixels in a pixelated integrated array, thereby achieving circular polarization imaging of a vector light field. This work

Please cite this article in press as: Liu et al., High-performance integrated circularly polarized light detection using soft-helix-decorated perovskite diodes, Newton (2024), https://doi.org/10.1016/j.newton.2024.100003

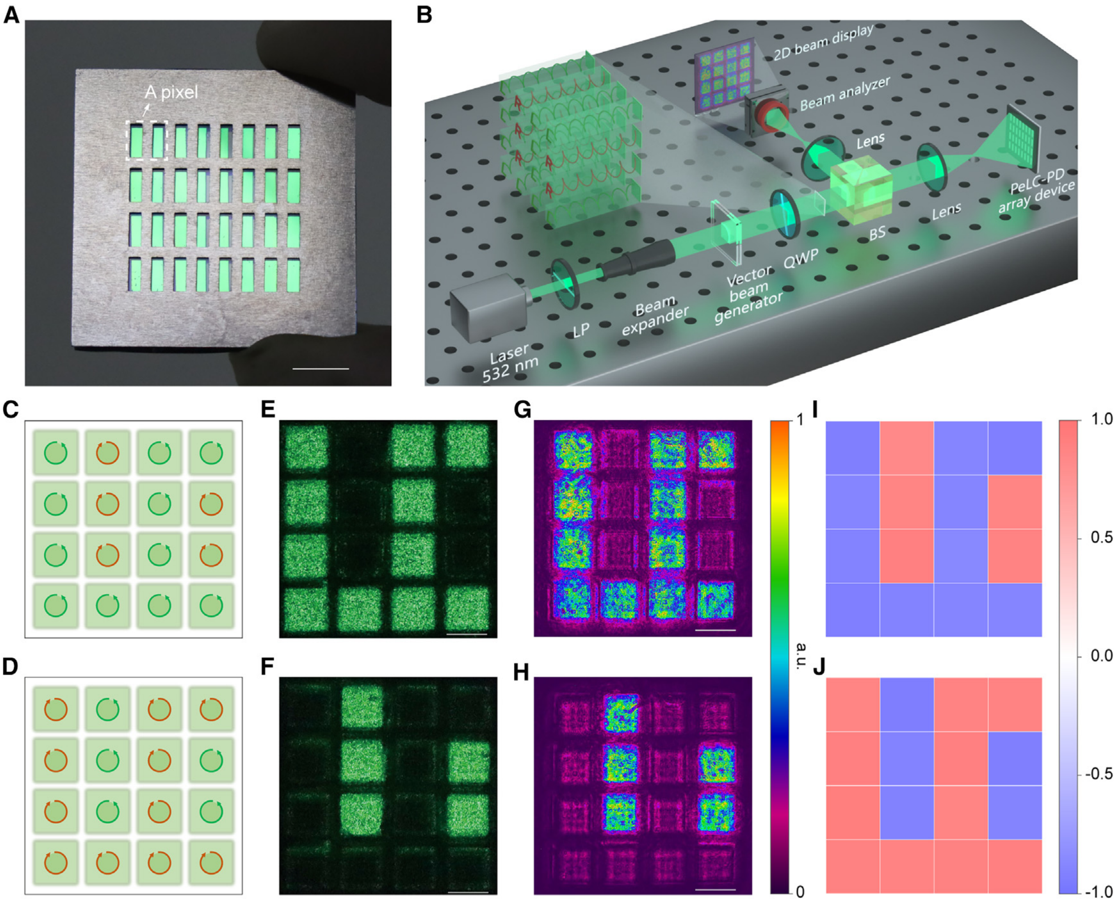

Figure 6. PeLC-PD array device for circular polarization imaging
(A) Photograph of the PeLC-PD array device. Scale bar: 5 mm.
(B) Schematic diagram of the circular polarization imaging by PeLC-PD array device.
(C and D) Illustration of spatial distribution of circular polarization states of the vector beam.
(E and F) Photographs of the vector beam detected by a CMOS camera through the left-handed circular polarizer. Scale bars: 3 mm.
(G and H) Profiles of the vector beam detected by a beam analyzer through the left-handed circular polarizer. Scale bars: 3 mm.
(I and J) Image results of the PeLC-PD array device under the vector beam.

combines the optical chirality selectiveness of a soft helix and the excellent optoelectronic performance of metal halide perovskite thin-film diodes to create a flexible and integrable polarization detector that is applicable to a wide spectral range, creating new opportunities for research and applications in many fields, such as chiroptics. These insights could drive the development of high-performance, integrated sensing and detection chips with superior sensitivity and accuracy.

METHODS

Characterizations

All characterizations of perovskite films, CLCs, and PeLC-PD devices are implemented at room temperature (25°C) to ensure the stability and consistency of the sample performance. EQE measurements were measured by the Newport-74125 system (Newport Instruments). EL images were then recorded using an industrial charge-coupled device (CCD) camera (MindVision) with a prime lens at 2 V forward bias. The CD spectra were collected on a JASCO-1500 CD spectrometer with a data pitch of 1 nm, a scanning rate of 500 nm/min, and a standard sensitivity mode. The photocurrent from the device was measured using a Keithley 2400 Source Meter at 0 V voltage. The polarized optical microscopy (POM) images of the CLC layer were observed under reflection mode and captured by a CCD camera (Nikon LVPOL 100). SEM images were obtained using a Helios G4 UC scanning electron microscope. All samples for SEM measurements were coated with 2 nm Au. The atomic force microscope images were obtained using a Horiba OmegaScope AFM scanning probe microscope (HORIBA Scientific). The UV-vis absorption spectra and transmittance spectra were recorded on a Shimadzu UV2600 spectrophotometer. The time-resolved photoluminescence (TRPL) spectra were performed with a Edinburgh Instruments Fluorescence Spectrometer FLS1000 applied with a pulsed excitation laser of 510 nm.

Please cite this article in press as: Liu et al., High-performance integrated circularly polarized light detection using soft-helix-decorated perovskite diodes, Newton (2024), https://doi.org/10.1016/j.newton.2024.100003

Calculation method

The optical transmittance of the CLC layer was calculated by the programmed code based on the 3D finite-difference time-domain (FDTD) method. The mesh accuracy was 2, and a perfectly matched layer was utilized in the z direction to prevent unwanted reflections, while periodic boundary conditions were employed in the x and y directions for all the calculations. The polarized light with arbitrary circular polarization can be achieved by combining a linear polarizer and a QWP with varying angles from 0° to 360° between the linear polarization direction and the fast axis. The simulation time was 5,000 fs, and the convergence criteria were set with an automatic shutoff minimum of 1×10^{-5}. The extraordinary refractive index n_e of nematic LC SLC1717 is 1.739 and ordinary refractive index n_o is 1.519 at a temperature of 20°C and a wavelength of 532 nm. The refractive index of SiO_2 is derived from Palik.

RESOURCE AVAILABILITY

Lead contact

Further information and requests for resources and reagents should be directed to and will be fulfilled by the lead contact, Wei-Hong Zhu (whzhu@ecust.edu.cn).

Materials availability

All the chemicals and reagents in this study were purchased and used directly without further purification. Patterned ITO glass, quartz, organic halide salts (FAI and MABr), PbI_2, and C_{60} were purchased from Advanced Election Technology. $PbBr_2$ was purchased from Macklin. CsI was purchased from Sigma-Aldrich. MACl and BCP were purchased from Tokyo Chemical Industry. PTAA and PEDOT:PSS were purchased from Xi'an Yuri Solar. All the anhydrous solvents were purchased from Acros Organics. Nematic LC SLC1717 was purchased from Shijiazhuang Slichem Display Material, LC monomer LC242 was purchased from Shanghai Haohong Scientific, chiral dopant *R*(*S*)-5011 was purchased from Hecheng Display, Irgacure 184 was purchased from Anhui Senrise Technologies, sulfonic azo dye SD1 was purchased from Dai-Nippon Ink and Chemicals, and ITO-coated PET substrate was purchased from Shanghai Mifang Electronic Technology.

Data and code availability

The published article includes all data analyzed during this study. Any additional information required to reanalyze the data reported in this paper is available from the lead contact upon request.

ACKNOWLEDGMENTS

The work was supported by the Basic Science Center of the National Natural Science Foundation (T2488302), the National Key Research and Development Program of China (2022YFA120370), the National Natural Science Foundation of China (22425502, 22338006, 92356301, and 22179037), the Innovation Program of the Shanghai Municipal Education Commission (15XD1501400 and 2021-01-07-00-02-E00107), the Shanghai Municipal Science and Technology Major Project (21JC1401700), the Shanghai Sailing Program (23YF1409000), the Program of Introducing Talents of Discipline to Universities (B16017), the "Shuguang Program" of the Shanghai Education Development Foundation and Shanghai Municipal Education Commission (21SG29), and the Fellowship of the China National Postdoctoral Program for Innovative Talents (BX20230125). Additional support was provided by the Feringa Nobel Prize Scientist Joint Research Center and the Research Center of Analysis and Test of East China University of Science and Technology.

AUTHOR CONTRIBUTIONS

Conceptualization, Y.W. and S.L.; methodology, S.L., X.L., H.H., and C.Y.; investigation, S.L., F.Y., H.Z., M.M., and H.G.; resources, X.L., F.Y., and S.Z.; writing—original draft, S.L.; writing—review & editing, Y.W., Z.Z., and W.-H.Z.; funding acquisition, Y.W., Z.Z., and W.-H.Z.; supervision, Y.W., Z.Z., and W.-H.Z.

DECLARATION OF INTERESTS

The authors declare no competing interests.

SUPPLEMENTAL INFORMATION

Supplemental information can be found online at https://doi.org/10.1016/j.newton.2024.100003.

Received: July 15, 2024
Revised: October 10, 2024
Accepted: November 25, 2024
Published: December 18, 2024

REFERENCES

1. Togan, E., Chu, Y., Trifonov, A.S., Jiang, L., Maze, J., Childress, L., Dutt, M.V.G., Sørensen, A.S., Hemmer, P.R., Zibrov, A.S., and Lukin, M.D. (2010). Quantum entanglement between an optical photon and a solid-state spin qubit. Nature *466*, 730–734.
2. Claborn, K., Puklin-Faucher, E., Kurimoto, M., Kaminsky, W., and Kahr, B. (2003). Circular dichroism imaging microscopy: application to enantiomorphous twinning in biaxial crystals of 1,8-dihydroxyanthraquinone. J. Am. Chem. Soc. *125*, 14825–14831.
3. Zhan, X., Zhou, Z., Zhou, W., Yan, Y., Yao, J., and Zhao, Y.S. (2023). Wavelength-tunable circularly polarized laser arrays for multidimensional information encryption. Adv. Opt. Mater. *11*, 2200872.
4. Rodríguez-Fortuño, F.J., Barber-Sanz, I., Puerto, D., Griol, A., and Martínez, A. (2014). Resolving light handedness with an on-chip silicon microdisk. ACS Photonics *1*, 762–767.
5. Schmidt, J., Guggenmos, A., Hofstetter, M., Chew, S.H., and Kleineberg, U. (2015). Generation of circularly polarized high harmonic radiation using a transmission multilayer quarter waveplate. Opt. Express *23*, 33564–33578.
6. Wan, L., Zhang, R., Cho, E., Li, H., Coropceanu, V., Brédas, J.-L., and Gao, F. (2023). Sensitive near-infrared circularly polarized light detection via non-fullerene acceptor blends. Nat. Photonics *17*, 649–655.
7. Yang, Y., Da Costa, R.C., Fuchter, M.J., and Campbell, A.J. (2013). Circularly polarized light detection by a chiral organic semiconductor transistor. Nat. Photonics *7*, 634–638.
8. Zhang, C., Xu, C., Chen, C., Cheng, J., Zhang, H., Ni, F., Wang, X., Zou, G., and Qiu, L. (2022). Optically programmable circularly polarized photodetector. ACS Nano *16*, 12452–12461.
9. Chen, C., Gao, L., Gao, W., Ge, C., Du, X., Li, Z., Yang, Y., Niu, G., and Tang, J. (2019). Circularly polarized light detection using chiral hybrid perovskite. Nat. Commun. *10*, 1927.
10. Yao, B., Wei, Q., Yang, Y., Zhou, W., Jiang, X., Wang, H., Ma, M., Yu, D., Yang, Y., and Ning, Z. (2023). Symmetry-broken 2D lead–tin mixed chiral perovskite for high asymmetry factor circularly polarized light detection. Nano Lett. *23*, 1938–1945.
11. Zhao, Y., Qiu, Y., Feng, J., Zhao, J., Chen, G., Gao, H., Zhao, Y., Jiang, L., and Wu, Y. (2021). Chiral 2D-perovskite nanowires for stokes photodetectors. J. Am. Chem. Soc. *143*, 8437–8445.
12. Ma, W., Xu, L., De Moura, A.F., Wu, X., Kuang, H., Xu, C., and Kotov, N.A. (2017). Chiral inorganic nanostructures. Chem. Rev. *117*, 8041–8093.
13. Wang, L., Xue, Y., Cui, M., Huang, Y., Xu, H., Qin, C., Yang, J., Dai, H., and Yuan, M. (2020). A chiral reduced-dimension perovskite for an efficient flexible circularly polarized light photodetector. Angew. Chem. Int. Ed. *59*, 6442–6450.

14. Wu, J., Zhang, X., You, S., Zhu, Z.K., Zhu, T., Wang, Z., Li, R., Guan, Q., Liang, L., Niu, X., and Luo, J. (2023). Low detection limit circularly polarized light detection realized by constructing chiral perovskite/Si heterostructures. Small *19*, 2302443.

15. Hu, R., Lu, X., Hao, X., and Qin, W. (2023). An organic chiroptical detector favoring circularly polarized light detection from near-infrared to ultraviolet and magnetic-field-amplifying dissymmetry in detectivity. Adv. Mater. *35*, 2211935.

16. Ishii, A., and Miyasaka, T. (2020). Direct detection of circular polarized light in helical 1D perovskite-based photodiode. Sci. Adv. *6*, eabd3274.

17. Zhu, D., Jiang, W., Ma, Z., Feng, J., Zhan, X., Lu, C., Liu, J., Liu, J., Hu, Y., Wang, D., et al. (2022). Organic donor-acceptor heterojunctions for high performance circularly polarized light detection. Nat. Commun. *13*, 3454.

18. Liu, Y., and Xing, P. (2023). Circularly polarized light responsive materials: design strategies and applications. Adv. Mater. *35*, 2300968.

19. Chen, Y., Zhang, Y., Li, H., Li, Y., Zheng, W., Quan, Y., and Cheng, Y. (2022). Dynamic circularly polarized luminescence with tunable handedness and intensity enabled by achiral dichroic dyes in cholesteric liquid crystal medium. Adv. Mater. *34*, 2202309.

20. Yang, X., Zhou, M., Wang, Y., and Duan, P. (2020). Electric-field-regulated energy transfer in chiral liquid crystals for enhancing upconverted circularly polarized luminescence through steering the photonic bandgap. Adv. Mater. *32*, 2000820.

21. Yang, X., Jin, X., Zhao, T., and Duan, P. (2021). Circularly polarized luminescence in chiral nematic liquid crystals: generation and amplification. Mater. Chem. Front. *5*, 4821–4832.

22. Bisoyi, H.K., and Li, Q. (2022). Liquid crystals: versatile self-organized smart soft materials. Chem. Rev. *122*, 4887–4926.

23. Broer, D.J., Lub, J., and Mol, G.N. (1995). Wide-band reflective polarizers from cholesteric polymer networks with a pitch gradient. Nature *378*, 467–469.

24. Mitov, M. (2012). Cholesteric liquid crystals with a broad light reflection band. Adv. Mater. *24*, 6260–6276.

25. Han, H., Lee, Y.J., Kyhm, J., Jeong, J.S., Han, J., Yang, M.K., Lee, K.M., Choi, Y., Yoon, T., Ju, H., et al. (2020). High-performance circularly polarized light-sensing near-infrared organic phototransistors for optoelectronic cryptographic primitives. Adv. Funct. Mater. *30*, 2006236.

26. Stranks, S.D., Wood, S.M., Wojciechowski, K., Deschler, F., Saliba, M., Khandelwal, H., Patel, J.B., Elston, S.J., Herz, L.M., Johnston, M.B., et al. (2015). Enhanced amplified spontaneous emission in perovskites using a flexible cholesteric liquid crystal reflector. Nano Lett. *15*, 4935–4941.

27. Ali, T., Elston, S.J., Lin, J., and Morris, S.M. (2023). On-Demand Polarization Controllable Liquid Crystal Laser. Adv. Mater. Technol. *8*, 2200674.

28. Li, M., Hu, H., Liu, B., Liu, X., Zheng, Z.-G., Tian, H., and Zhu, W.-H. (2022). Light-reconfiguring inhomogeneous soft helical pitch with fatigue resistance and reversibility. J. Am. Chem. Soc. *144*, 20773–20784.

29. Liu, X., Yuan, C., Sun, P., Na, Z., Hu, H., and Zheng, Z. (2024). Programming dual-color circularly polarized luminescence with self-organized soft photonic helix. Laser Photon. Rev. *18*, 2300603.

30. He, Y., Lin, S., Guo, J., and Li, Q. (2021). Circularly polarized luminescent self-organized helical superstructures: from materials and stimulus-responsiveness to applications. Aggregate *2*, e141.

31. Yun, Y., Han, G.S., Park, G.N., Kim, J., Park, J., Vidyasagar, D., Jung, J., Choi, W.C., Choi, Y.J., Heo, K., et al. (2022). A wide bandgap halide perovskite based self-powered blue photodetector with 84.9% of external quantum efficiency. Adv. Mater. *34*, 2206932.

32. Miao, J., and Zhang, F. (2019). Recent progress on highly sensitive perovskite photodetectors. J. Mater. Chem. C *7*, 1741–1791.

33. Fei, C., Li, N., Wang, M., Wang, X., Gu, H., Chen, B., Zhang, Z., Ni, Z., Jiao, H., Xu, W., et al. (2023). Lead-chelating hole-transport layers for efficient and stable perovskite minimodules. Science *380*, 823–829.

34. Guo, H., Liu, C., Hu, H., Zhang, S., Ji, X., Cao, X.-M., Ning, Z., Zhu, W.-H., Tian, H., and Wu, Y. (2023). Neglected acidity pitfall: boric acid-anchoring hole-selective contact for perovskite solar cells. Natl. Sci. Rev. *10*, nwad057.

35. Zhang, S., Ye, F., Wang, X., Chen, R., Zhang, H., Zhan, L., Jiang, X., Li, Y., Ji, X., Liu, S., et al. (2023). Minimizing buried interfacial defects for efficient inverted perovskite solar cells. Science *380*, 404–409.

36. Lin, Q., Armin, A., Nagiri, R.C.R., Burn, P.L., and Meredith, P. (2015). Electro-optics of perovskite solar cells. Nat. Photonics *9*, 106–112.

37. Lin, Q., Armin, A., Burn, P.L., and Meredith, P. (2015). Filterless narrowband visible photodetectors. Nat. Photonics *9*, 687–694.

38. Maes, J., Balcaen, L., Drijvers, E., Zhao, Q., De Roo, J., Vantomme, A., Vanhaecke, F., Geiregat, P., and Hens, Z. (2018). Light absorption coefficient of $CsPbBr_3$ perovskite nanocrystals. J. Phys. Chem. Lett. *9*, 3093–3097.

39. Zhu, T., Wu, H., Ji, C., Zhang, X., Peng, Y., Yao, Y., Ye, H., Weng, W., Lin, W., and Luo, J. (2022). Polar photovoltaic effect in chiral alternating cations intercalation-type perovskites driving self-powered ultraviolet circularly polarized light detection. Adv. Opt. Mater. *10*, 2200146.

40. Wei, J., Chen, Y., Li, Y., Li, W., Xie, J., Lee, C., Novoselov, K.S., and Qiu, C.-W. (2023). Geometric filterless photodetectors for mid-infrared spin light. Nat. Photonics *17*, 171–178.

41. Shang, X., Wan, L., Wang, L., Gao, F., and Li, H. (2022). Emerging materials for circularly polarized light detection. J. Mater. Chem. C *10*, 2400–2410.

42. Kim, I., Jang, J., Kim, G., Lee, J., Badloe, T., Mun, J., and Rho, J. (2021). Pixelated bifunctional metasurface-driven dynamic vectorial holographic color prints for photonic security platform. Nat. Commun. *12*, 3614.

43. Schaefer, B., Collett, E., Smyth, R., Barrett, D., and Fraher, B. (2007). Measuring the stokes polarization parameters. Am. J. Phys. *75*, 163–168.

44. Zheng, Z., Hu, H., Zhang, Z., Liu, B., Li, M., Qu, D.-H., Tian, H., Zhu, W.-H., and Feringa, B.L. (2022). Digital photoprogramming of liquid-crystal superstructures featuring intrinsic chiral photoswitches. Nat. Photonics *16*, 226–234.

45. Huang, Y., Zhou, Y., Doyle, C., and Wu, S.-T. (2006). Tuning the photonic band gap in cholesteric liquid crystals by temperature-dependent dopant solubility. Opt. Express *14*, 1236–1242.

46. Wang, Q., Bao, J., Zhang, Y., Wang, Y., Qiu, D., Yang, J., Zhang, J., Gao, H., Wu, Y., Dong, H., et al. (2024). High-performance organic narrow dual-band circular polarized light detection for encrypted communications and color imaging. Adv. Mater. *36*, 2312396.

NEWTON, Volume *1*

Supplemental information

High-performance integrated circularly polarized light detection using soft-helix-decorated perovskite diodes

Shuaijun Liu, Furong Yu, Xuan Liu, Huidong Zhang, Minyi Ma, Shuo Zhang, Huanxin Guo, Honglong Hu, Conglong Yuan, Zhigang Zheng, Yongzhen Wu, and Wei-Hong Zhu

Contents

1. Supplemental Methods

2. Supplemental Figures and Tables

1. Supplemental Methods

1.1 Fabrication of rigid and flexible perovskite photodiodes

Glass/ITO and PET/ITO substrates were sequentially cleaned with soapy water, deionized water, and ethanol, by sonication for 20 min in each solution. Then the cleaned substrates were treated with UV ozone for 15 min before used. The PEDOT:PSS solution was prepared with a concentration of 1.3-1.7 wt% in H_2O. The PTAA solution was prepared with a concentration of 2.5 mg mL^{-1} in chlorobenzene. MPA-CPA were dissolved in anhydrous ethanol at a concentration of 1.0 mg mL^{-1}. The as-prepared solution was spin coated on the glass / ITO substrates at 3000 rpm for 30 s in a nitrogen filled glovebox. After annealing on a hotplate at 100°C for 10 min, the HTL coated substrates were cooled down to room temperature.

The "FAMA" perovskite precursor was prepared by mixing 1.4 M $FAPbI_3$ and $MAPbBr_3$ perovskite precursor in DMF : DMSO (4 : 1 volume ratio, v : v) with 9% PbX_2 excess respectively (X = I or Br) in a volume ratio of 95 : 5. Then, 40 μL of CsI solution in DMSO (1.5 M) was mixed with 960 μL of the above-mentioned "FAMA" solution. Additionally, 15 mol% MACl was added to the perovskite precursor solution resulting in triple cation perovskite precursor. 70 μL of the perovskite precursor was spin-coated onto the HTL coated ITO substrates (1.5 cm × 2.0 cm) at 4000 rpm for 40 s (5 s acceleration to 4000 rpm). 200 μL mixed antisolvent (chlorobenzene : isopropanol = 9 : 1, v : v, containing 0.5 mM F-PEAI) was slowly dripped onto the center of the film at 7 s before the end of spinning program. The perovskite film was obtained by annealing at 100°C for 60 min. After the perovskite deposition, 20 nm of C_{60}, 7 nm of BCP and 100 nm of silver electrode were thermally evaporated. The area of each perovskite photodiode is 0.09 cm^2.

1.2 Fabrication of rigid PeLC-PDs

The quartz substrates were sequentially washed with deionized water, ethanol, and acetone for 30 min with sonication. The substrates were further cleaned with UV ozone treatment for 20 min before used. Sulfonic azo dye SD1 solution was spin-coated onto the substrates under ambient atmospheric conditions and annealed at 100°C for 10 min to remove DMF. Subsequently, three adhesive tapes were stuck on the left, middle and right of the quartz, and covered the ITO substrate with perovskite photodiode. Noted that it is vital to make sure the close fit of two quartz. Then, the cell was irradiated under ultraviolet polarized light for 5 min. Different amounts of chiral dopant *S*-5011 or *R*-5011 (weight ratio to SLC1717) was added into SLC1717 and was stirred at 100°C for 2 h. Finally, SLC1717 with *S*- and *R*-5011 were loaded into the left and right cell in the PeLC-PD by capillary action, respectively.

1.3 Fabrication of flexible PeLC-PDs

The quartz substrates were sequentially washed with deionized water, ethanol, and acetone for 30 min with sonication. The substrates were further cleaned with UV ozone treatment for 20 min before used. Sulfonic azo dye SD1 solution was spin-coated onto the substrates under ambient atmospheric conditions and annealed at 100°C for 10 min to remove DMF. Subsequently, the adhesive tape was sticked on another quartz, and cover the quartz substrate with SD1 coated. Noted that it is vital to make sure the close fit of two quartz. Then, the cell was irradiated under ultraviolet polarized light for 5 min. Different amounts of chiral dopant *S*-5011 or *R*-5011 (weight ratio to LC242) were added into LC242 and stirred at 100°C for 2 h. The mixture was loaded into the cell by capillary action and polymerized by ultraviolet exposure for 20 min. The cell was peeled off to obtain an individual chiral LC polymer film. Finally, a flexible PeLC-PD device was achieved by simply sticking the LC polymer film onto the incident side of perovskite photodiode.

1.4 Fabrication of integrated PeLC-PD array

The customized ITO substrates were sequentially washed with deionized water, ethanol, and acetone for 30 min with sonication. The substrates were further cleaned with UV ozone treatment for 20 min before used. The Perovskite photodiode was fabricated by the same method mentioned above. The area of each perovskite photodiode is 0.03 cm^2. Sulfonic azo dye SD1 solution was spin-coated onto an ITO substrate under ambient atmospheric conditions and annealed at 100°C for 10 min to remove DMF. Subsequently, nine adhesive tapes were stuck on the ITO substrate, and cover the ITO substrate with perovskite photodiode. Then, the cell was irradiated under ultraviolet polarized light for 5 min. 2.8% chiral dopant *S*-5011 or *R*-5011 (weight ratio to SLC1717) was added into LC242 and was stirred at 100°C for 2 h. The *S*-handed and *R*-handed mixture was loaded into the cell by capillary action in an alternating order. Finally, a metal mask was covered on the ITO substrate.

1.5 Characterization of the different polarization states by Poincaré sphere

To measure the Stokes parameters *S* (see S_0, S_1, S_2, S_3 in Scheme 2), firstly, detecting the intensity I_1, I_2, I_3 at different angles $\alpha = 0$, 45°, and 90° while removing the QWP ($\beta = 0$), respectively.

$$I_1\ (\beta = 0,\ \alpha = 0) = 1/2\ (S_0 + S_1) \quad \text{(Equation S1)}$$

$$I_2\ (\beta = 0,\ \alpha = 45^o) = 1/2\ (S_0 + S_2) \quad \text{(Equation S2)}$$

$$I_3\ (\beta = 0,\ \alpha = 90^o) = 1/2\ (S_0 - S_1) \quad \text{(Equation S3)}$$

Then, detecting the intensity I_4 as inserting the QWP at different angles $\beta = 90°$, $\alpha = 45°$.

$$I_4\ (\beta = 90^o,\ \alpha = 45^o) = 1/2\ (S_0 + S_3) \quad \text{(Equation S4)}$$

Finally, calculating the Stokes parameters from the four equations below.

$$S_0 = (I_1 + I_3) \quad \text{(Equation S5)}$$

$$S_1 = (I_1 - I_3) \quad \text{(Equation S6)}$$

$$S_2 = 2I_2 - (I_1 + I_3) \quad \text{(Equation S7)}$$

$$S_3 = 2I_4 - (I_1 + I_3) \quad \text{(Equation S8)}$$

In general, the light beam is not completely polarized, so the degree of polarization, denoted by *γ*, is employed to quantify this property. It can be defined as follows:

$$\gamma = \frac{\sqrt{{S_1}^2 + {S_2}^2 + {S_3}^2}}{S_0}$$

(Equation S9)

Where, $0 < \gamma \leq 1$. This means that partially polarized light can be expressed as a sum of completely polarized light and unpolarized light.

$$\begin{pmatrix} S_0 \\ S_1 \\ S_2 \\ S_3 \end{pmatrix} = (1-\gamma)\begin{pmatrix} S_0 \\ 0 \\ 0 \\ 0 \end{pmatrix} + \gamma\begin{pmatrix} S_0 \\ S_1/\gamma \\ S_2/\gamma \\ S_3/\gamma \end{pmatrix}$$

(Equation S10)

When $\gamma=1$, it means that the light is completely polarized and can be expressed on the Poincaré spherical surface. Therefore, the north pole (0, 0, 1) represents right-handed polarization while the south pole (0, 0, -1) represents left-handed polarization.

2. Supplemental Figures and Tables

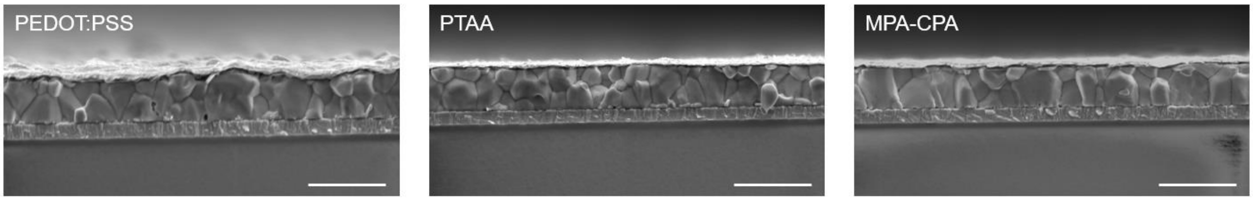

Figure S1. Cross-sectional scanning electron microscopy (SEM) images of perovskite photodiodes based on PEDOT:PSS, PTAA, and MPA-CPA, respectively. Scale bars: 1 μm. Related to Figure 2.

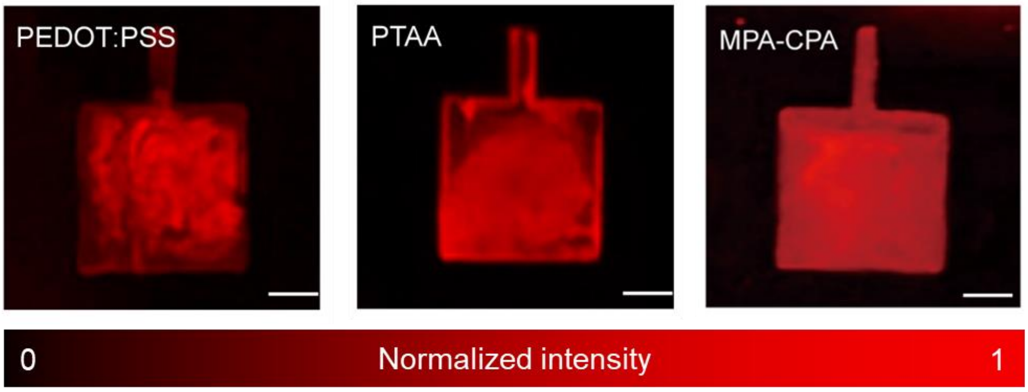

Figure S2. Electroluminescence (EL) imaging of perovskite photodiodes based on different HTLs at 2 V forward bias, scale bars: 1 mm. The perovskite photodiodes based on MPA-CPA exhibit much more uniform emission than that of PEDOT:PSS and PTAA. Related to Figure 2.

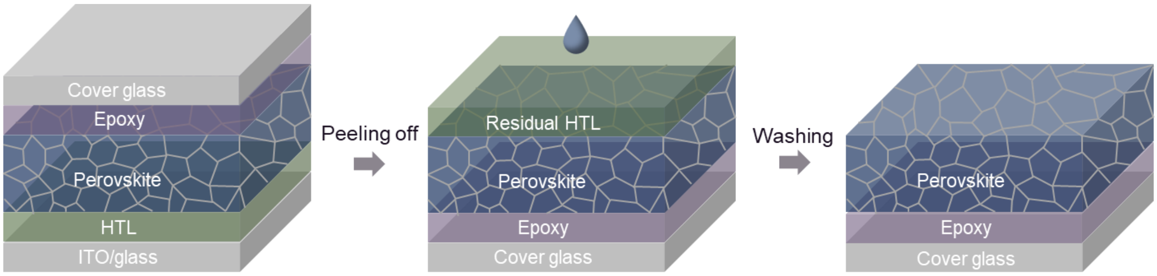

Figure S3. Illustration of the peeling off process for perovskite film. The perovskite film was covered with an epoxy coated cover glass, followed by ultraviolet light illumination for 20 s. The bottom perovskite surface was obtained by peeling off and washing with chlorobenzene to remove the residual HTL. Related to Figure 2.

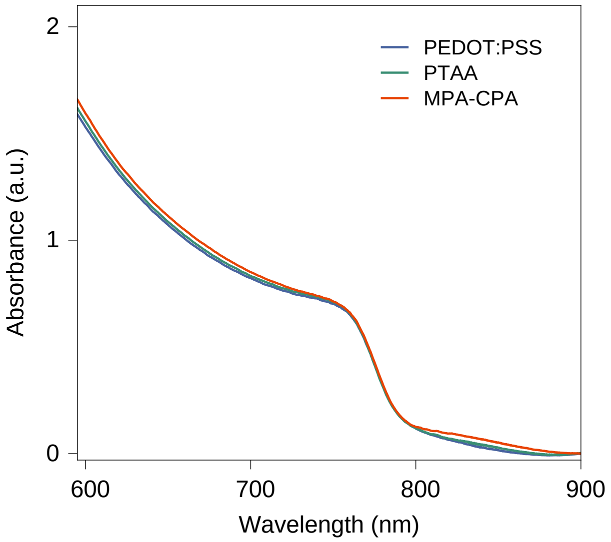

Figure S4. Absorption spectra of the bottom surface of perovskite films based on PEDOT:PSS, PTAA, and MPA-CPA. It shows negligible differences in the absorption of perovskite films based on three different types of HTLs, which may reveal that the variation in perovskite films on these HTLs lies in defects density at the bottom surface between the perovskite film and HTL, which further leads to the nonradiative recombination and affects EQE performance of the entire device. Related to Figure 2.

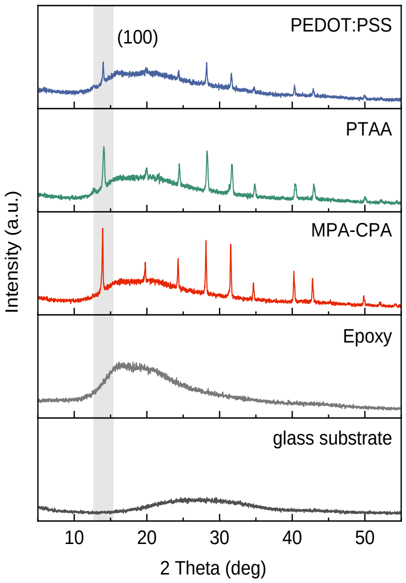

Figure S5. XRD patterns of perovskite films deposited on PEDOT:PSS, PTAA and MPA-CPA, measured from the bottom side using the peeled-off samples. Related to Figure 2.

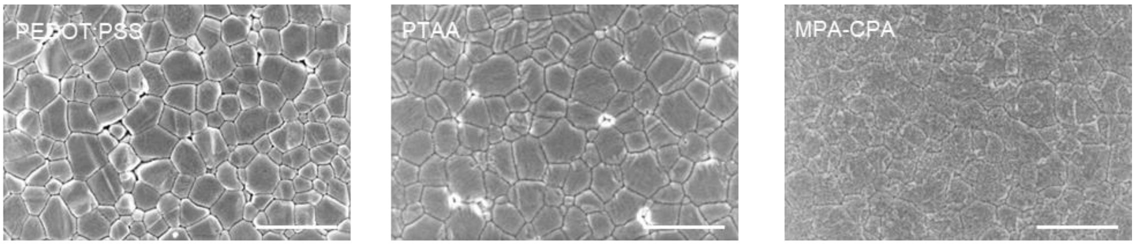

Figure S6. Top-view SEM images of the exposed bottom surface of perovskite films deposited on PEDOT:PSS, PTAA and MPA-CPA, scale bars: 1 μm. Obvious voids along with grain boundaries are observed in PEDOT:PSS and PTAA-based perovskite films, while the MPA-CPA-based film exhibits compact and uniform morphology. Related to Figure 2.

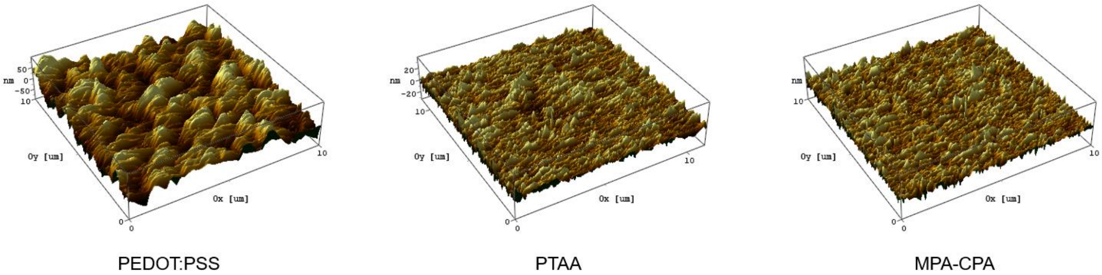

Figure S7. AFM images of the exposed bottom surface of perovskite deposited on PEDOT:PSS, PTAA, and MPA-CPA, showing roughness of 22.01, 4.52, and 4.41 nm (obtained from root-mean-square), respectively. Related to Figure 2.

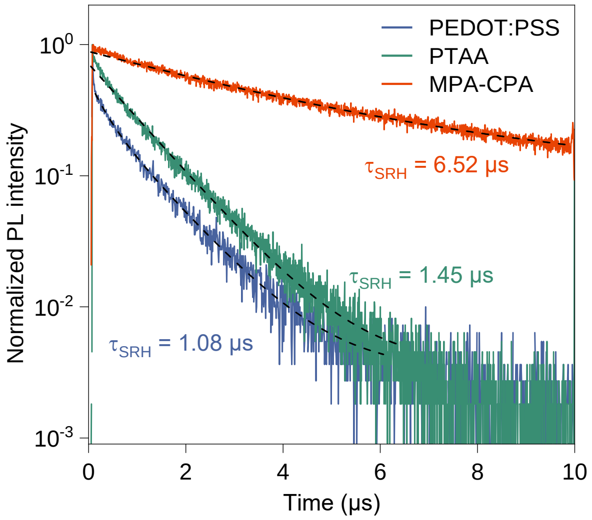

Figure S8. Time-resolved PL decay at 790 nm of perovskite film based on three different HTLs with the EPL excitation at 510 nm. Related to Figure 2.

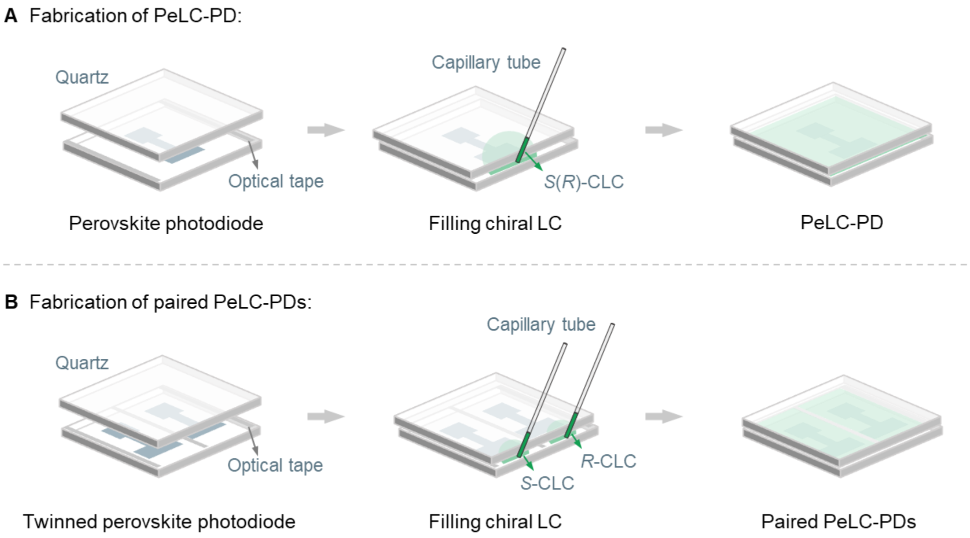

Figure S9. Schematic diagram of fabrication process for (A) single PeLC-PD and (B) paired PeLC-PD devices. Related to Figure 3.

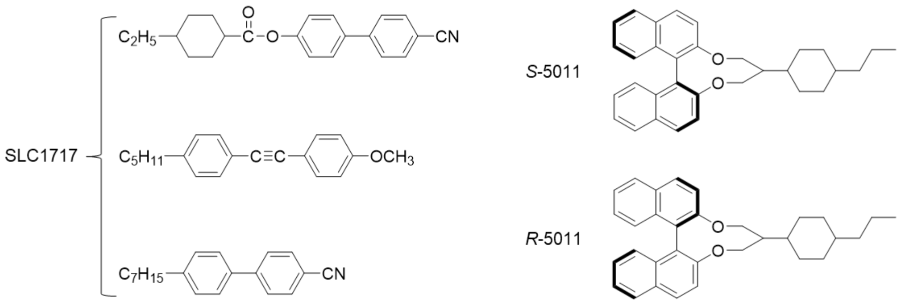

Figure S10. Molecular structures of nematic liquid crystal SLC1717 and chiral dopant *S*(*R*)-5011. Related to Figure 3.

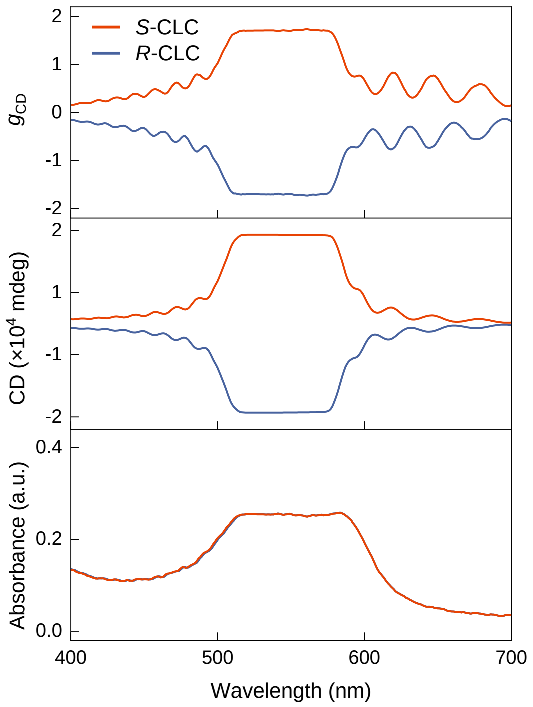

Figure S11. g_{CD} spectra of the chiral LC layer. Related to Figure 3.

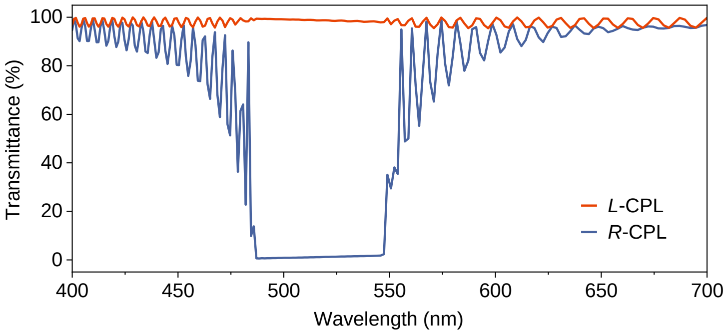

Figure S12. Simulated transmittance spectra of *R*-CLC under the *L*- and *R*-CPL. Related to Figure 3.

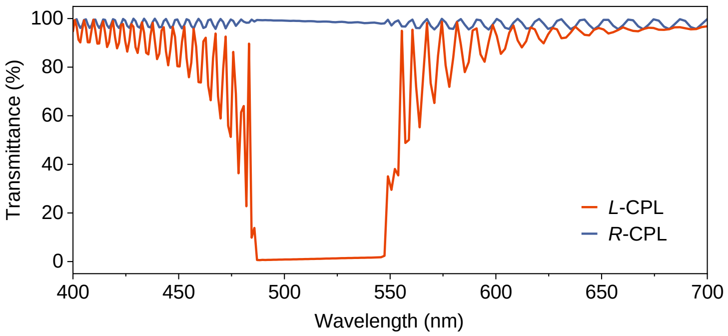

Figure S13. Simulated transmittance spectra of *L*-CLC under the *L*- and *R*-CPL. Related to Figure 3.

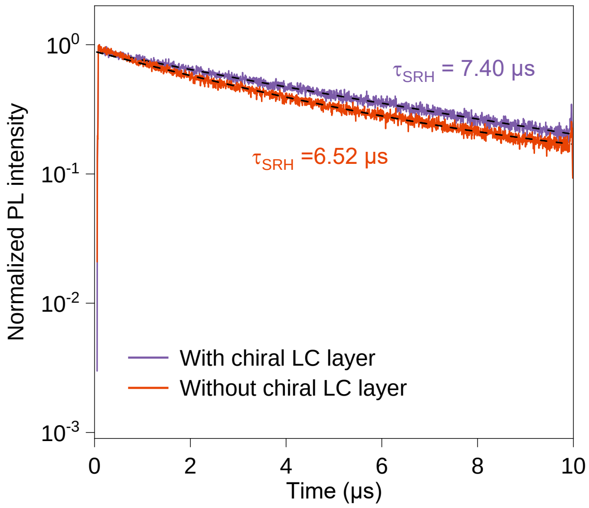

Figure S14. Time-resolved PL decay at 790 nm of perovskite film with and without chiral LC layer. Related to Figure 3.

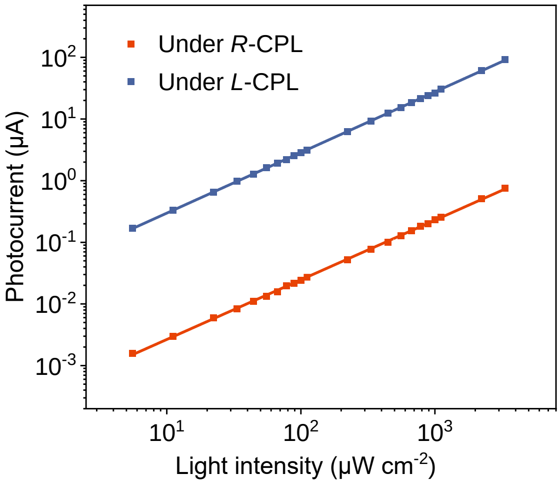

Figure S15. Photocurrent recorded by the green light responsive PeLC-PD based on *R*-CLC under *L*- and *R*-CPL with varied intensity from 10^{-1} to 10^3 μW cm^{-2} at 0 V bias, which is generated from a beam of 532-nm laser followed by a linear polarizer and a QWP. Related to Figure 3.

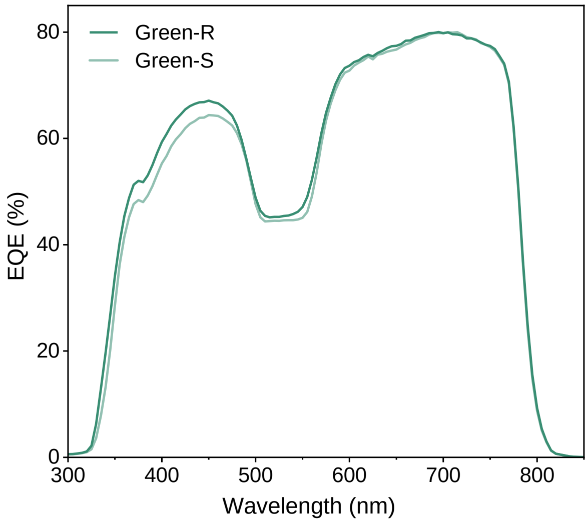

Figure S16. External quantum efficiency (EQE) spectra of green light responsive paired PeLC-PDs. Related to Figure 4.

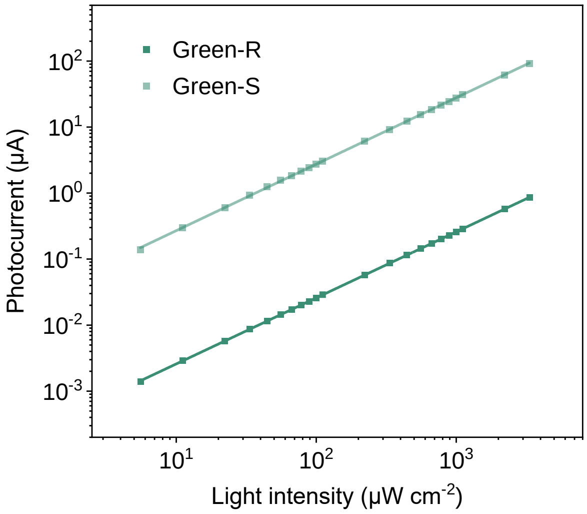

Figure S17. Photocurrent recorded by the green light responsive paired PeLC-PDs under a beam of 532-nm *R*-CPL with various intensity from 10^{-1} to 10^{3} μW cm^{-2} at 0 V bias. Related to Figure 4.

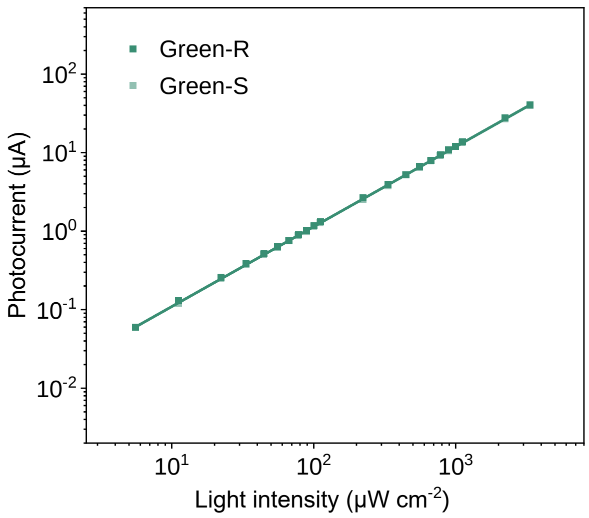

Figure S18. Photocurrent recorded by the green light responsive paired PeLC-PDs based on *R*(*S*)-CLC under a beam of 532-nm linearly polarized light (LPL) with varied intensity from 10^{-1} to 10^{3} μW cm^{-2} at 0 V bias. Related to Figure 4.

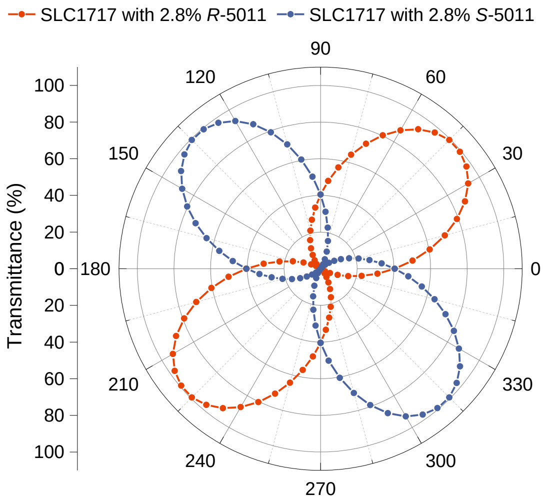

Figure S19. Simulated transmittance of SLC1717 with 2.8% *R*(*S*)-5011 under varied polarization states, which was achieved by changing the angle between a linear polarizer and a QWP from 0° to 360°. Related to Figure 4.

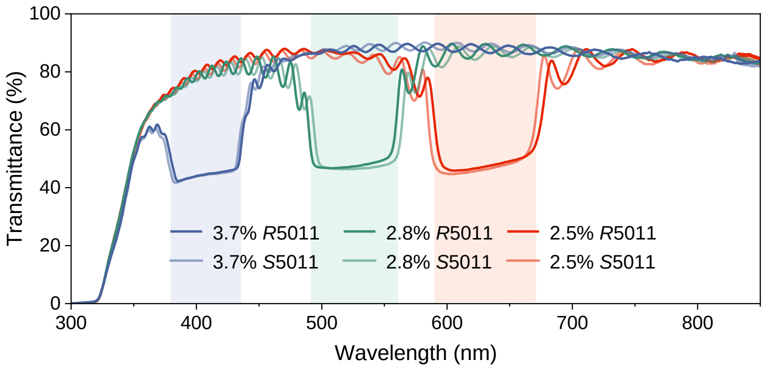

Figure S20. Transmittance spectra of chiral LC layers that are prepared with different concentration of chiral dopant (*R*- or *S*-5011). Related to Figure 5. It is worth noting that the concentration of the chiral dopant significantly affects the wavelength position of photonic bandgap in chiral LC, which stems from its variable pitch length. The relation between chiral dopant concentration (c) and photonic bandgap wavelength (λ_p) can be expressed by the equation $\lambda_p = \bar{n}/(c \cdot HTP)$, where $\bar{n}$, and HTP refer to the average refractive index of LC, helical twisting power, respectively. As the concentration of the chiral dopant increases, the twist in the LC intensifies, leading to a shortening of the pitch length and a blueshift of the photonic bandgap.

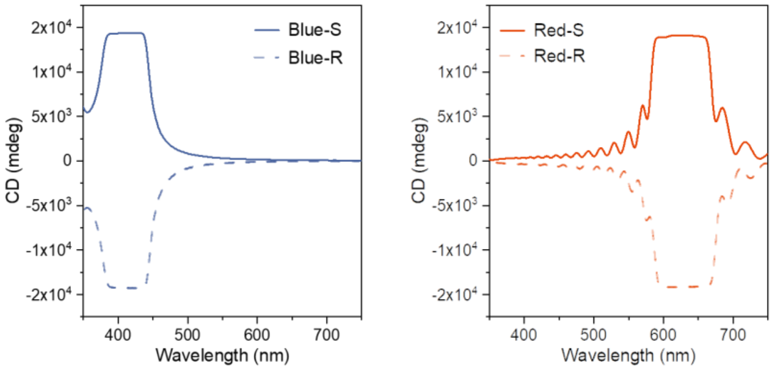

Figure S21. Circular dichroism (CD) spectra of blue and red light responsive PeLC-PDs. Related to Figure 5.

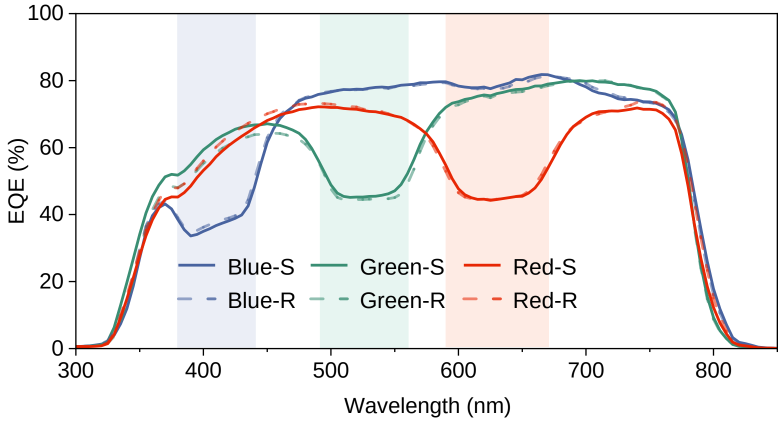

Figure S22. EQE spectra of blue, green and red light responsive PeLC-PDs. Related to Figure 5.

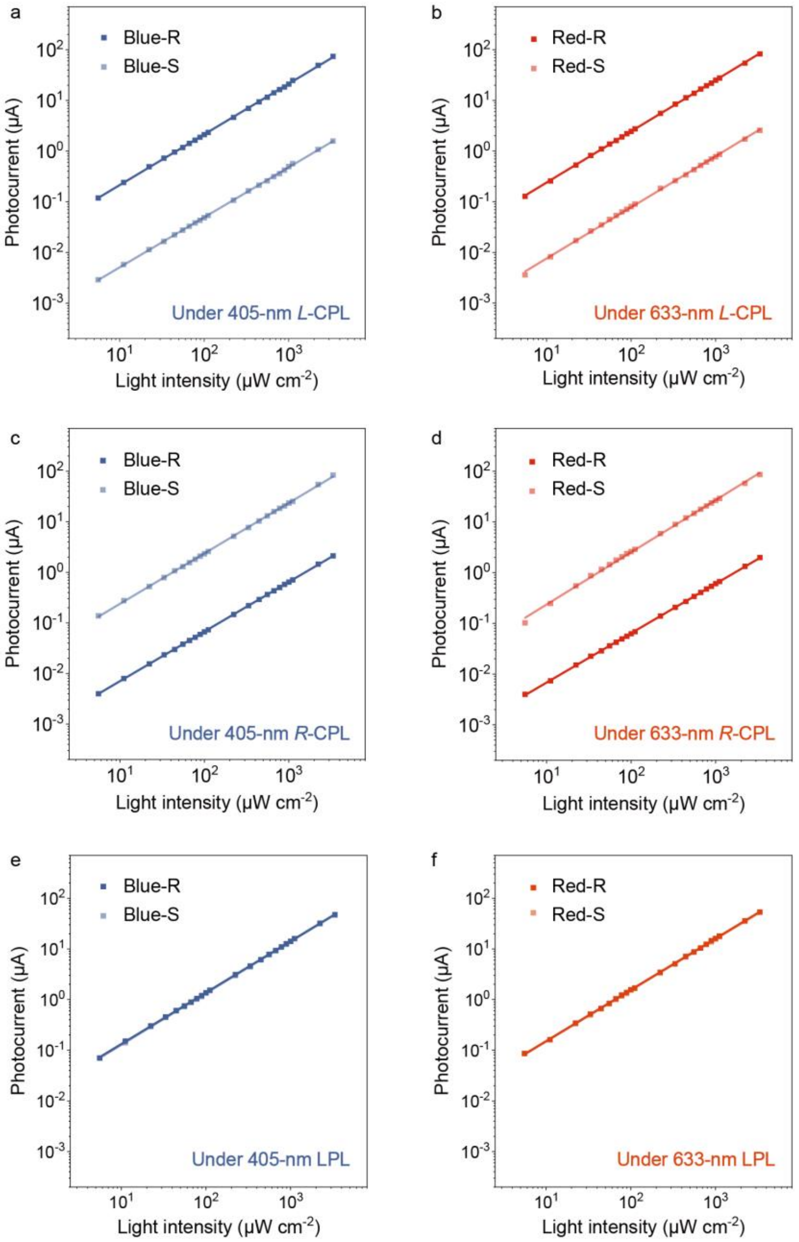

Figure S23. Photocurrent recorded by the blue and red light responsive paired PeLC-PDs at 0 V bias under a beam of 405-nm and 633-nm (a, b) *L*-CPL, (c, d) *R*-CPL, and (e, f) LPL with varied intensity from 10^{-1} to 10^{3} μW cm^{-2}. Related to Figure 5.

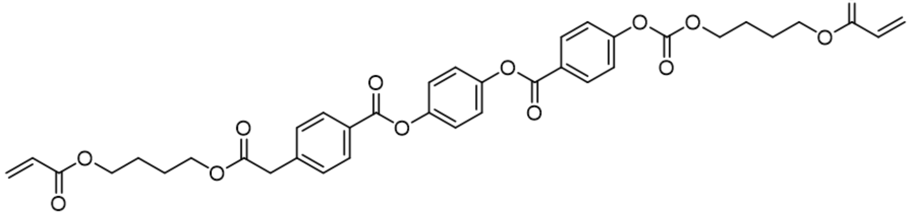

LC242

Figure S24. Molecular structure of nematic LC monomer LC242. Related to Figure 5.

Figure S25. Photographs of flexible blue, green, and red light responsive PeLC-PDs. The devices were fabricated by simply sticking the individual LC polymer films onto the incident side of the perovskite photodiode. Scale bars: 5 mm. Related to Figure 5.

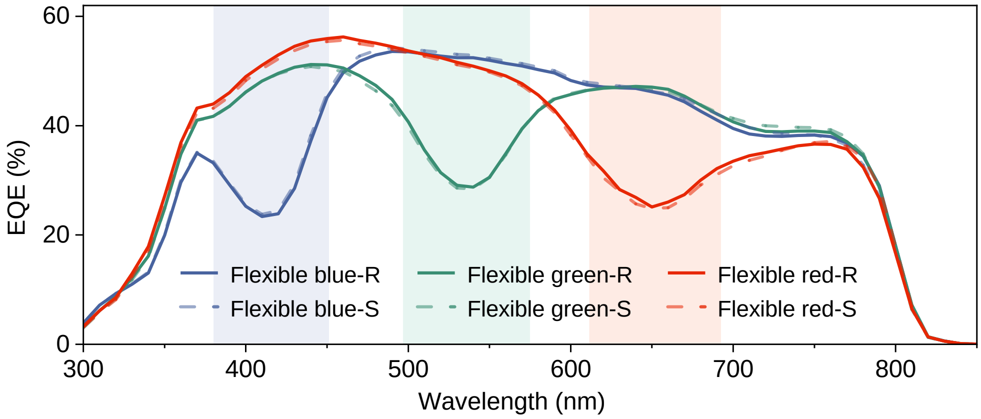

Figure S26. EQE spectra of flexible blue, green, and red light responsive PeLC-PD. Related to Figure 5.

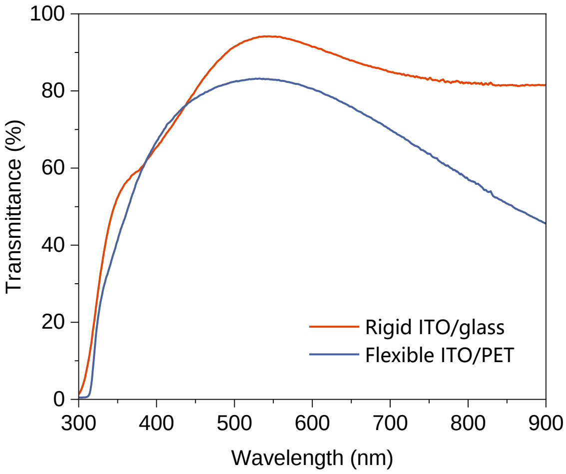

Figure S27. Transmittance spectra of rigid ITO/glass and flexible IEO/PET substrates used in this work. Related to Figure 5.

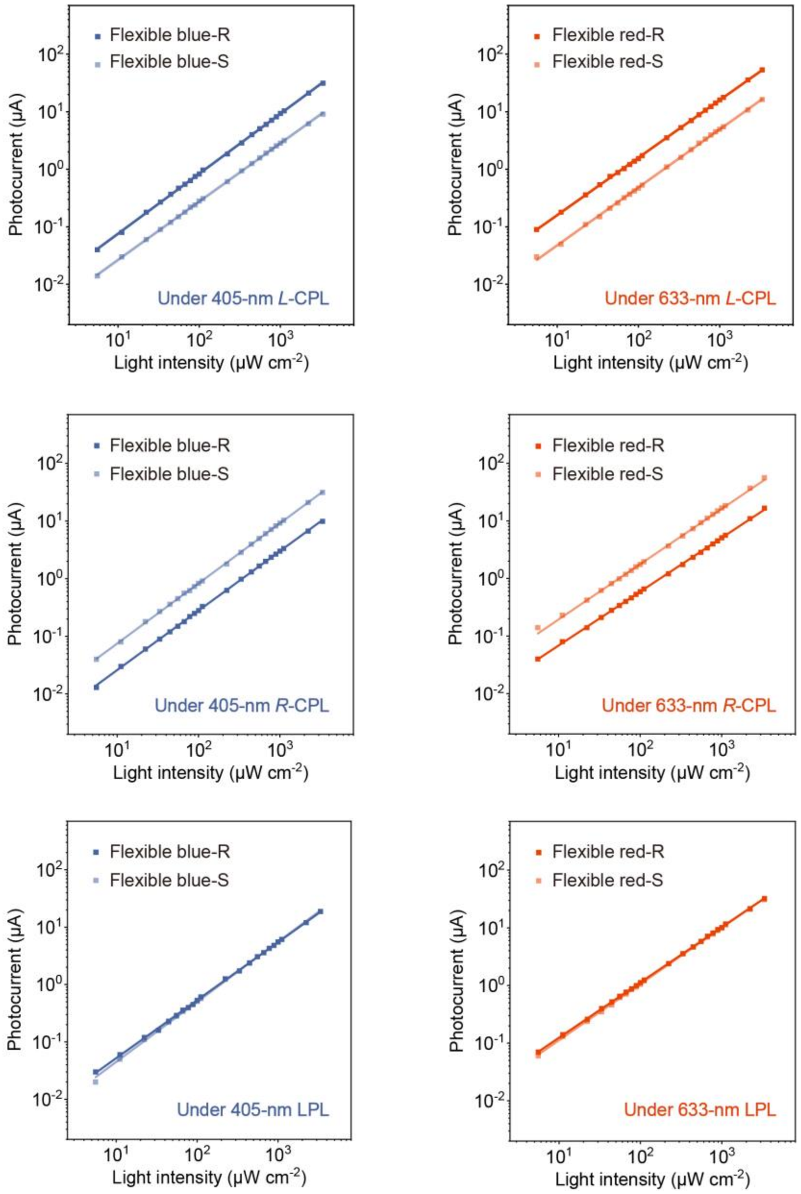

Figure S28. Photocurrent recorded by the flexible blue and red light responsive PeLC-PDs at 0 V bias under a beam of 405-nm and 633-nm (a, b) *L*-CPL, (c, d)*R*-CPL, and (e, f)LPL with varied intensity from 10^{-1} to 10^{3} μW cm^{-2}. Related to Figure 5.

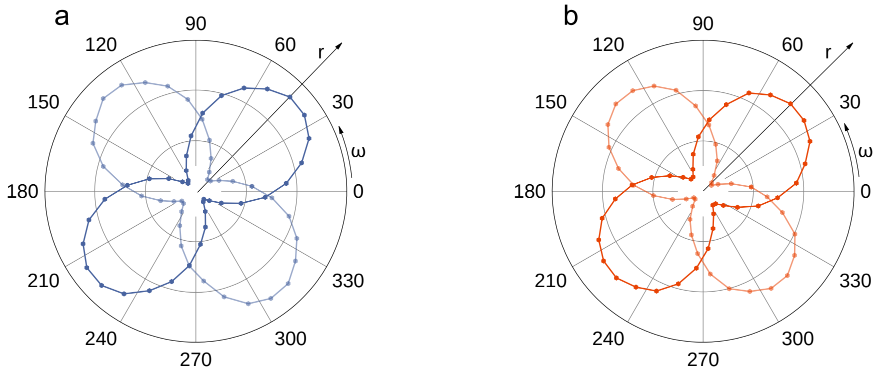

Figure S29. Polarization-dependent photocurrent recorded by the flexible blue and red light responsive PeLC-PDs in a polar coordinate system. Dark and dash line refer to the photocurrent from PeLC-PD based on *R*-CLC at right and *S*-CLC at left side, respectively. Related to Figure 5.

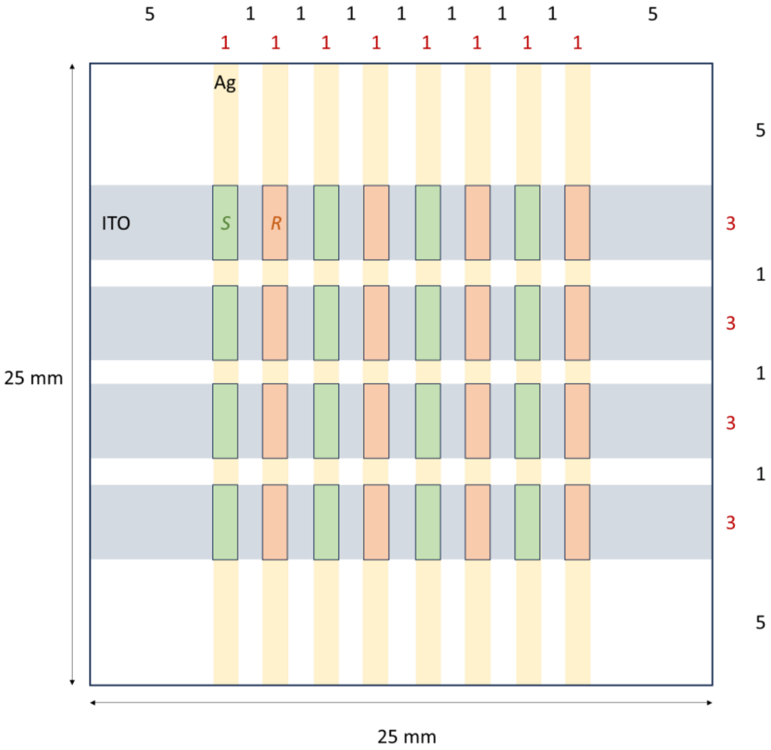

Figure S30. Schematic illustration of the PeLC-PD array. Related to Figure 6.

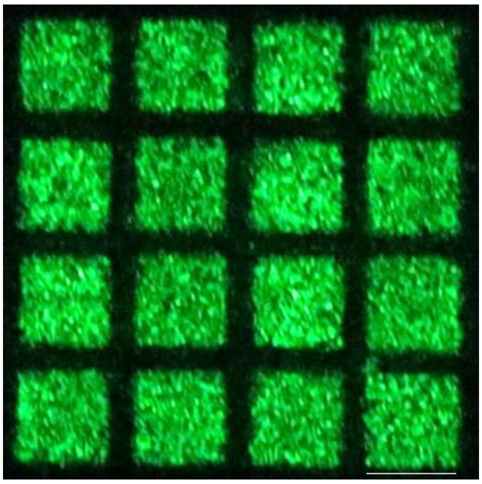

Figure S31. Photograph of vector beam detected by a CMOS camera. Scale bars: 3 mm. Related to Figure 6.

Table S1. Responsivity (R) and linear dynamic range (LDR) of the blue, green, and red light responsive paired PeLC-PDs under *L*(*R*)-CPL at 405 nm, 532 nm, and 633 nm, respectively. Related to Figure 3 and 5.

Wavelength of incident light (nm)		405		532		633	
Circular polarization state of incident light		LCP	RCP	LCP	RCP	LCP	RCP
Responsivity (mA W^{-1})	*S*	6	260	2	291	9	294
	R	234	7	294	3	278	7
LDR (dB)	*S*	52	55	55	56	57	58
	R	57	54	56	55	56	54

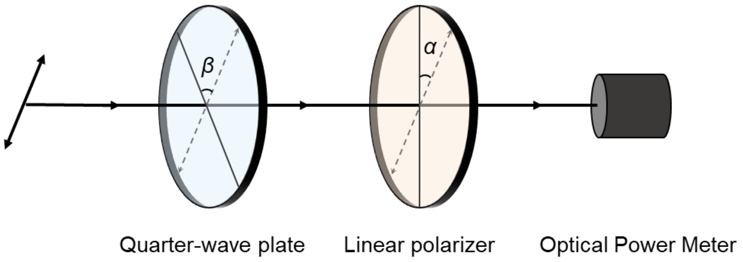

Scheme 1. Illustration of measuring the Stokes parameters. The incident light, after traversing the quarter-wave plate (QWP) and linear polarizer oriented at angles *β* and *α*, respectively, was detected in terms of intensity using an optical power meter.[1,2]

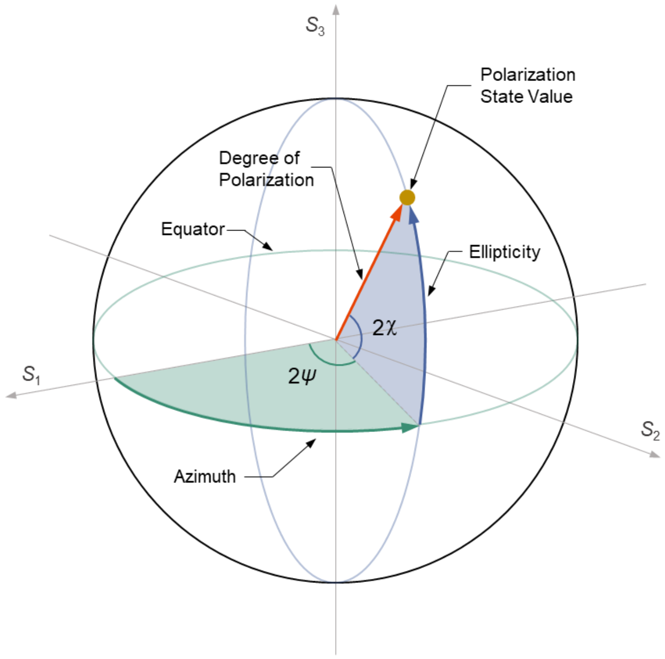

Scheme 2. Description of polarization states of light.

References

1. Schaefer, B., Collett, E., Smyth, R., Barrett, D., and Fraher, B. (2007). Measuring the stokes polarization parameters. Am. J. Phys. *75*, 163–168.

2. Tyo, J.S., Goldstein, D.L., Chenault, D.B., and Shaw, J.A. (2006). Review of passive imaging polarimetry for remote sensing applications. Appl. Opt. *45*, 5453.